A three-dimensional finite element formulation coupling electrochemistry and solid mechanics on resolved microstructures of all-solid-state lithium-ion batteries

Christoph P. Schmidt [a],[*], Stephan Sinzig [a],[b], Volker Gravemeier [c], Wolfgang A. Wall [a]

[a] *TUM School of Engineering and Design, Department of Engineering Physics and Computation, Institute for Computational Mechanics, Technical University of Munich, Boltzmannstraße 15, 85748 Garching bei München, Germany*
[b] *TUMint.Energy Research GmbH, Lichtenbergstraße 4, 85748 Garching bei München, Germany*
[c] *AdCo Engineering^{GW} GmbH, Bahnhofstraße 18, 85774 Unterföhring, Germany*

A R T I C L E   I N F O

A B S T R A C T

In this paper we present an all-solid-state lithium-ion battery (ASSB) model that considers electrochemistry and solid mechanics in a fully coupled manner. The model spatially resolves the three-dimensional microstructure of an ASSB cell and is based on non-linear continuum mechanics. The coupling of electrochemistry and solid mechanics is incorporated via lithiation-dependent volumetric changes of the active materials and the consistent formulation of the electrochemical governing equations on deformed geometries resulting in changed percolation paths. As the volumetric changes due to (de-)lithiation are reported to be large for several active materials, we introduce this effect using a multiplicative split of the deformation gradient. To also allow for large deformations in the mass conservation equation, an Arbitrary Lagrangian–Eulerian formulation is employed. Furthermore, we show the central steps to deduce the finite element formulation of our model as well as the adopted monolithic solution procedure to solve this strongly coupled non-linear problem. The linear solver used for large problem setups is adjusted from the advanced, physics-oriented preconditioning technique published in our previous work. In the numerical examples, we investigate three different geometries with up to about 1.3 million degrees of freedom and thereby prove that our approach is applicable to geometrically large and complex scenarios. Moreover, we show that our approach consistently introduces the mass and charge conservation on deformed meshes. Furthermore, the numerical examples demonstrate the high relevance to incorporate current collectors into the ASSB cell simulations. Finally, we show that solid mechanics and the coupling effects have indeed a large impact on the ASSB cell performance and their incorporation is therefore vital for precise results and predictions.

1. Introduction

In many applications, such as stationary energy storage systems, as well as electric or hybrid vehicles lithium-ion batteries (LIB) play a key role. However, both the energy density and fast charging capability of conventional LIB is limited and will soon reach its physical limits [1,2]. Currently, all-solid-state lithium-ion batteries (ASSB) are promising an essential step forward as they are expected

---

* Corresponding author.
E-mail address: christoph.schmidt@tum.de (C.P. Schmidt).

to feature high power and energy density while also meeting crucial safety standards. Though, there are also several challenges associated with the ASSB technology being targeted by current research. Since all components of the battery are solid bodies, and the active materials are subject to volume changes during (de-)lithiation, the interaction of electrochemistry and solid mechanics has substantial influence on the performance [3–5]. This highlights that single-field investigations, i.e. isolated investigations of electrochemical or solid mechanical properties, are not sufficient to generate a detailed understanding of the system. Moreover, the energy density compared to conventional LIB can only be increased by up to 70% if the lithium metal anode can be enabled by the usage of solid electrolytes [6].

A multitude of *ex situ*, *in situ* as well as *in operando* experimental studies investigating the interaction of electrochemistry and solid mechanics in ASSB have been published in recent years. As most of the quantities or effects of interest are not easily accessible to experimental investigations, often a multitude of different analysis tools are applied. Those include but are not restricted to differential electrochemical mass spectrometry (DEMS) [7], digital image correlation (DIC) [8,9], electrochemical impedance spectroscopy (EIS) [7,10–12], neutron imaging [13], pressure monitoring [5,7], scanning electron microscopy (SEM) [7,10,12], time-of-flight secondary ion mass spectrometry (ToF-SIMS) [7], x-ray computed tomography (CT) [14], and x-ray photoelectron spectroscopy (XPS) [7,11,12,15]. Usually, such complex machinery is expensive, time-consuming, or not even available to most of the research community. Even with all those tools some important open questions remain. Thus, numerical simulations in combination with theoretical findings gain more and more attention as they enable valuable insights for reasonable effort [16].

Yet, due to the high complexity of physical effects that are relevant in ASSB also most of the existing simulation approaches base on various simplifications, either concerning the considered physical phenomena, or the geometry they can be applied to. Therefore, those simulation models do not necessarily enable reliable predictions, nor profound analysis of the occurring phenomena. Recently, elaborate microstructure resolved models describing electrochemical processes but neglecting solid mechanics [17,18] have been proposed. Furthermore, a multitude of simulation methods considering electrochemistry and solid mechanics are published. Some of those methods rely on linear mechanics [19–27] that assume small deformations and strains. For materials whose volume change can be up to some hundred percent upon full (de-)lithiation [28,29] this simplification is not justified anymore. Others present very sophisticated modeling approaches but only apply them to simple geometries [30–34], one-dimensional problems [35], two-dimensional geometries [36,37], or single particles [38–40]. Hence, the underlying geometric complexity is simplified and thereby local phenomena like inhomogeneous current density distributions, concentration distributions, or mechanical stresses, all of which can have a significant impact on the system performance, are neglected. Another common approach is to rely on spatial homogenization, e.g. when Newman-type pseudo 2D models are their basis [41–43]. Again, while useful for certain investigations, such models are consequently not capable to capture local effects in ASSB.

This work introduces a novel computational framework for an analysis of electrochemistry, solid mechanics and their coupling effects in ASSB. In particular, we present a three-dimensional nonlinear continuum model discretized by the finite element method. It resolves the porous microstructure and local physical phenomena without spatial homogenization. The formulation of the solid mechanics is derived from nonlinear continuum mechanics and thus capable of capturing large deformations. As the solid mechanics and the electrochemistry are coupled, the ability to account for large deformations in the solid mechanics field needs to be considered in the electrochemistry as well to assure a consistent formulation. Therefore, mass and charge conservation are formulated using an Arbitrary Lagrangian–Eulerian (ALE) approach to enable the solution on moving meshes due to deformations as provided by the solid mechanics field. All equations are treated in a monolithic fashion to maximize computational robustness and efficiency of the solution algorithm. To this end, we also extend the advanced, physics-oriented block preconditioning and solution techniques from our previous work [44] to the resulting linear systems of equations. Combined with the full MPI parallelization of our implementation, our model thus opens up new possibilities for large-scale, high-performance computations in settings with strict demands on accuracy. Thereby, we bridge the existing gap in literature by enabling the solution of the presented complex coupled nonlinear model on realistic microstructure resolved setups of ASSB.

The remainder of this paper is structured as follows: In Section 2 we describe the continuous mathematical model including all governing equations as well as the coupling of electrochemistry and solid mechanics. Furthermore, the interface, boundary, and initial conditions are presented. Section 3 focuses on numerical aspects concerning the employed finite element formulation and the nonlinear solution procedure of the discretized monolithic system. Moreover, in Section 4 we outline the setup of the presented numerical examples including information on the geometries, materials, and operating conditions used to run the simulations. We verify that our model conserves mass and charge on deforming meshes, discuss the relevance of current collectors in ASSB modeling, and apply our model to a realistic geometry of an ASSB cell to compare the electrochemical results to published data from [18], and thereby show the applicability of the approach to geometrically large problems. Furthermore, we present that the consideration of the coupled problem influences the system and is thus vital to obtain precise results. Additionally, the influence of the mechanical setup on the performance of ASSB cells is analyzed, and local mechanical effects are shown. Lastly, Section 5 summarizes the presented work and the deduced insights before ideas for future research based on this work are discussed.

2. Problem definition

The interdependence of the solid mechanics and the electrochemical fields are of particular importance within ASSB as already motivated in the introduction. In the following we will formulate the conservation of angular and linear momentum for solid mechanics, as well as the conservation of charge and mass for electrochemistry. In addition, we will specify the coupling between fields and interfacial phenomena between domains. We start with characterizing the domains, interfaces and boundaries of interest of an ASSB cell.

2.1. Definition of domains, interfaces and boundaries of an ASSB cell

For many investigations it is possible to assume the cell to be symmetric in lateral direction, meaning that we are only considering a statistically representative extract of the real cell geometry which obviously reduces computational costs. For ease of presentation, a simplified 2D scheme of an ASSB cell is depicted in Fig. 1 to show its geometric properties.

The anode phase Ω_a and the cathode phase Ω_c constitute the active material phase of the electrodes $\Omega_{ed} = \Omega_a \cup \Omega_c$, whereas the electrolyte phase is split into a part depicting the "Solid Electrolyte Separator" $\Omega_{el,SES}$, and a part representing the electrolyte within the "Composite Cathode" $\Omega_{el,CC}$. Furthermore, the current collectors at the anode side and at the cathode side are depicted by $\Omega_{cc,a}$ and $\Omega_{cc,c}$, respectively. Additionally, we define the whole computational domain using $\Omega = \Omega_{cc,a} \cup \Omega_a \cup \Omega_{el,SES} \cup \Omega_{el,CC} \cup \Omega_c \cup \Omega_{cc,c}$. The interface of the anode and the electrolyte is given by $\Gamma_{a,el}$, while between the cathode and the electrolyte it is depicted by $\Gamma_{c,el}$. Besides, the interface between the solid electrolyte separator and the electrolyte of the composite cathode is represented by $\Gamma_{el,SES-CC}$, and the contact surface between the anode and the anode side current collector $\Gamma_{cc,a}$ is presented. Moreover, the interface of the composite cathode and the cathode side current collector is split into two disjoint parts. Herein, $\Gamma_{cc,c}$ denotes the contact surface between the cathode phase and the cathode side current collector, whereas $\Gamma_{cc,el}$ symbolizes the interface between the electrolyte and the current collector. On top of that, we introduce the outer boundary of the current collectors using $\Gamma_{cc,a-o}$ and $\Gamma_{cc,c-o}$ as well as the boundary due to the symmetric cut $\Gamma_{cut} = \partial\Omega \setminus (\Gamma_{cc,a-o} \cup \Gamma_{cc,c-o})$ of the real ASSB cell. To limit the complexity of the investigation we do not consider additional phases like the binder, or carbon black in this study. Even though the modeling approach does easily allow for different electrolytes in different parts of the ASSB as depicted in Fig. 1, for the moment we restrict ourselves to only one electrolyte phase here ($\Omega_{el} = \Omega_{el,SES} \cup \Omega_{el,CC}$) to not unnecessarily increase the complexity of the notation with limited additional insight. However, it is straightforward to account for more than one electrolyte materials in order to e.g. analyze hybrid cell concepts. The time interval of interest is represented by $t \in [0, t^{end}]$.

2.2. Conservation equations

In this subsection we begin with presenting the modeling equations for the solid mechanics field. To retain validity of our proposed model also for large deformations, we base it on the principles of nonlinear continuum mechanics. Finally, we elaborate on the equations describing the electrochemical field, that are solved on deforming geometries to enable a consistent solution of the coupled problem.

2.2.1. Solid mechanics: conservation of linear and angular momentum

For the mathematical description of the solid mechanics problem a bijective mapping $\varphi_t : X \mapsto x$ that assigns every point X in the material configuration for a given time t to the corresponding point x in the current configuration has to be introduced. Now we describe the deformation of the body by the deformation gradient $F = \frac{\partial x}{\partial X}$ and apply the conservation of linear momentum resulting in the equation of nonlinear elasto-dynamics (see e.g. [45] for details):

$$\nabla_X \cdot (F \cdot S) + b_0 = \rho_0 \ddot{u}_{def} \qquad \text{in} \Omega_0 \times [0, t^{end}], \tag{1}$$

where $\nabla_X \cdot$ denotes the material divergence operator, S the second Piola–Kirchhoff stress tensor, b_0 a body force per unit volume in the reference configuration, ρ_0 the mass density in the reference configuration, and $u_{def}(X, t) = x(X, t) - X$ the displacements due to a deformation of the body.

As reported by several publications, the volume of the active materials changes depending on their lithiation state (e.g. [5,46,47]). Since this change in volume can be up to some hundred percent upon full (de-)lithiation [28,29] a nonlinear treatment is required to correctly model this behavior. Therefore, we multiplicatively split the deformation into a part considering pure elasticity F_{el} and a part accounting for inelastic, stress-free volume changes F_{in}:

$$F = F_{el} \cdot F_{in}. \tag{2}$$

Fig. 1. Schematic sketch of the computational domain.

By considering a hyperelastic material law and the common assumption that only elastic strains result in stresses, we obtain the second Piola–Kirchhoff stress tensor S as the partial derivative of the elastic strain energy function Ψ_{el} w.r.t. the elastic right Cauchy–Green tensor $C_{el} = F_{el}^T \cdot F_{el}$ as follows [48]:

$$S = 2 \, det F_{in} F_{in}^{-1} \cdot \frac{\partial \Psi_{el}}{\partial C_{el}} \cdot F_{in}^{-T} \qquad in \Omega_0 \times \left[0, t^{end}\right]. \tag{3}$$

Finally, the Cauchy stress tensor σ is obtained by the subsequent mapping of the second Piola–Kirchhoff stress tensor:

$$\sigma = (det F)^{-1} F \cdot S \cdot F^T \qquad in \Omega \times \left[0, t^{end}\right]. \tag{4}$$

Both, the Cauchy stress tensor and the second Piola–Kirchhoff stress tensor are symmetric $\sigma = \sigma^T$; $S = S^T$, resulting from the conservation of angular momentum [49]. Therefore, the balance of angular momentum is already implicitly ensured by the symmetry of those tensors and must not be considered separately. For further information on that topic we refer to [45,49].

2.2.2. Electrochemistry: conservation of charge

We start with the formulation of the charge conservation in a generic form based on the balance at an infinitesimal volume element:

$$\frac{\partial \rho}{\partial t} + \nabla \cdot i = 0 \qquad in \Omega \times \left[0, t^{end}\right], \tag{5}$$

with the charge density ρ, and the current density i. The electroneutrality condition states that no free charges accumulate at any point in space or time and is formulated as follows:

$$\sum_i z_i c_i = 0 \qquad in \Omega \times \left[0, t^{end}\right], \tag{6}$$

with the charge number z_i and the concentration c_i of the corresponding species i. It is known to be satisfied besides a thin space charge layer of some nanometers near the interfaces of the active materials [50,51]. As we are not considering the effect of space charge layers in this work, the electroneutrality conditions holds true within the whole ASSB cell. Consequently, there is no accumulation of free charges, resulting in the following form of the charge conservation equation:

$$\nabla \cdot i = 0 \qquad in \Omega \times \left[0, t^{end}\right]. \tag{7}$$

As electrons are the only mobile charge carriers within the electrodes and the current collectors, we use Ohm's law to relate the current density to the electric field:

$$i = -\sigma \nabla \Phi \qquad in \Omega \setminus \Omega_{el} \times \left[0, t^{end}\right], \tag{8}$$

with the electronic conductivity σ, and the electric potential Φ resulting in the modeling equation for charge conservation within the electrodes and the current collectors:

$$\nabla \cdot (-\sigma \nabla \Phi) = 0 \qquad in \Omega \setminus \Omega_{el} \times \left[0, t^{end}\right]. \tag{9}$$

Inside the electrolyte the current density arises only due to the motion of ions. Faraday's law connects the mass flow of ions with the corresponding flux of charges:

$$i = F \sum_i z_i N_i, \tag{10}$$

with the Faraday constant F, and the flux N_i of species i. The flux is modeled to obey a Nernst–Planck equation describing the flux of charged species and incorporating the effects of convection, diffusion, and migration:

$$N_i = c_i \dot{u} - D_i \nabla c_i - \frac{z_i F D_i}{RT} c_i \nabla \Phi, \tag{11}$$

with the velocity $\dot{u}$, the diffusion coefficient D_i of species i, the universal gas constant R, and the temperature T. This results in the following generic form of the current density within the electrolyte:

$$i = F \left(\dot{u} \sum_i z_i c_i - \sum_i z_i D_i \nabla c_i - \sum_i \frac{z_i^2 F D_i}{RT} c_i \nabla \Phi \right). \tag{12}$$

Due to the electroneutrality condition presented in Eq. (6) the first sum of Eq. (12) vanishes. Moreover, several publications show that most solid electrolytes feature a lithium-ion transference number close to unity, meaning that lithium-ions are the only mobile ions within the solid electrolyte [52–54]. Again, in combination with the electroneutrality condition this means that no gradients in concentration emerge. Thus, also the second sum in Eq. (12) cancels out, resulting in the following formulation for the electrolyte

current density:

$$\boldsymbol{i} = -\kappa \nabla \Phi \qquad \text{in} \Omega_{\text{el}} \times \left[0, t^{\text{end}}\right], \tag{13}$$

where the ionic conductivity is denoted by $\kappa = \sum_i \frac{z_i^2 F D_i}{RT} c_i$. Inserting this into the general charge conservation Eq. (7), we end up with the charge conservation within the solid electrolyte:

$$\nabla \cdot \left(-\kappa \nabla \Phi\right) = 0 \qquad \text{in} \Omega_{\text{el}} \times \left[0, t^{\text{end}}\right]. \tag{14}$$

2.2.3. Electrochemistry: conservation of mass

The mass conservation of lithium is enforced within the computational domain of the ASSB. As the current collectors are modeled to be impermeable to lithium or lithium-ions, they are not taking part in the exchange of lithium and are therefore not considered in this subsection. Again, we begin with presenting a generic version of the mass conservation equation based on the balance at an infinitesimal volume element:

$$\frac{\partial c}{\partial t} + \nabla \cdot \boldsymbol{N} = 0 \qquad \text{in} \Omega_{\text{ed}} \cup \Omega_{\text{el}} \times \left[0, t^{\text{end}}\right], \tag{15}$$

where c denotes the concentration of lithium or lithium-ions and N the corresponding flux, modeled as already shown in Eq. (11). Without loss of generality, we split the velocity $\dot{\boldsymbol{u}}$ into its contributions as follows:

$$\dot{\boldsymbol{u}} = \dot{\boldsymbol{u}}_{\text{def}} + \dot{\boldsymbol{u}}_{\text{conv}}, \tag{16}$$

where $\dot{\boldsymbol{u}}_{\text{def}}$ and $\dot{\boldsymbol{u}}_{\text{conv}}$ denote the velocity due to a deformation of the bodies and the velocity due to convection, respectively. As all parts of the ASSB are solids, we demand the convective velocity to vanish:

$$\dot{\boldsymbol{u}}_{\text{conv}} = \boldsymbol{0}. \tag{17}$$

To also account for deformations caused by large volumetric changes, we reformulate the mass conservation equation to an ALE formulation. Therefore, we introduce an intermediate configuration – the so called ALE-configuration – moving with the deformation of the bodies. The partial time derivative from Eq. (15) is consequently rewritten to incorporate the total time derivative $\frac{\partial *}{\partial t}\big|_X$ as follows:

$$\frac{\partial c}{\partial t} = \frac{\partial c}{\partial t}\bigg|_X - \dot{\boldsymbol{u}}_{\text{def}} \cdot \nabla c. \tag{18}$$

By substituting the flux formulation as presented in Eq. (11), applying the product rule on the convective part of the divergence term from Eq. (15), as well as considering the mapping of the time derivative (see Eq. (18)) into Eq. (15), we arrive at the generic mass conservation in ALE formulation:

$$\frac{\partial c}{\partial t}\bigg|_X + c\nabla \cdot \dot{\boldsymbol{u}}_{\text{def}} - \nabla \cdot (D\nabla c) - \nabla \cdot \left(\frac{zFD}{RT} c\nabla \Phi\right) = 0 \qquad \text{in} \Omega_{\text{ed}} \cup \Omega_{\text{el}} \times \left[0, t^{\text{end}}\right]. \tag{19}$$

Now we start tailoring this equation to the electrode and electrolyte domain as shown in Fig. 1. In the electrodes we solve for the mass conservation of lithium. Hence, the charge number equals zero ($z = 0$) and we do not have to take migration effects into account. The mass conservation thus reads:

$$\frac{\partial c}{\partial t}\bigg|_X + c\nabla \cdot \dot{\boldsymbol{u}}_{\text{def}} - \nabla \cdot (D\nabla c) = 0 \qquad \text{in} \Omega_{\text{ed}} \times \left[0, t^{\text{end}}\right]. \tag{20}$$

Finally, we derive the mass conservation of lithium-ions within the solid electrolyte based on Eq. (19). We already know from the derivation of the charge conservation within the solid electrolyte that no gradients in concentration of lithium-ions arise. Thus, the third term of Eq. (19) equals zero. Furthermore, after applying the divergence to the fourth term it also vanishes (see Appendix A for details) resulting in the following form of the mass conservation equation:

$$\frac{\partial c}{\partial t}\bigg|_X + c\nabla \cdot \dot{\boldsymbol{u}}_{\text{def}} = 0 \qquad \text{in} \Omega_{\text{el}} \times \left[0, t^{\text{end}}\right]. \tag{21}$$

2.3. Coupling of the solid mechanics and electrochemical fields

One considered coupling effect is already described in the previous section by the solution of the electrochemical conservation equations of charge and mass on deforming geometries represented by Eq. (9), (14), (20) and (21).

Another considered coupling effect is the lithiation state dependent volume change of the active materials. These volume changes can be divided into two main groups, one that features an isotropic, and one that is represented by an anisotropic change in volume. Therefore, we formulated isotropic and anisotropic volume change models that can be flexibly applied to all domains. However, in the following we only elucidate the approaches that are relevant for the upcoming parts of the paper. Throughout this work, the cathode

side active material consists of secondary particles of NMC materials. Since the primary particles constituting the secondary particles can be assumed to be randomly distributed [55], we model the volume change of the cathode active material to be isotropic. Furthermore, we found that the following ansatz is capable of accurately representing published data as e.g. presented in [5] (cf. Fig. 2):

$$\boldsymbol{F}_{\mathrm{in}} = \left(\frac{f(\chi)+1}{f(\chi_0)+1} \right)^{1/3} \boldsymbol{I} \qquad \mathrm{in}\, \Omega_{\mathrm{c}} \times \left[0, t^{\mathrm{end}} \right], \tag{22}$$

where $f(\chi) = \frac{\Delta V}{V_{\mathrm{ref}}} = \frac{V(\chi) - V(\chi_{\mathrm{ref}})}{V(\chi_{\mathrm{ref}})}$ is a fit to published data of the volume change over lithiation state $\chi = \frac{c}{c_{\mathrm{max}}} \chi_{\mathrm{max}} det\boldsymbol{F}$. Herein, c_{max} is the maximum concentration of lithium inside the electrode and χ_{max} the corresponding lithiation state. Besides, V_{ref} and χ_{ref} describe the volume and lithiation state at the reference point for the measurement, respectively. Additionally, the lithiation state in the reference configuration, i.e. at the beginning of the simulation is denoted by χ_0.

For the current study we assume that no dendrites form at the anode side, as e.g. experimentally investigated by [56]. Instead, we assume that lithium is homogeneously deposited and dissolved at the anode electrolyte interface. The volume change of the anode is thus modeled to be anisotropic as follows:

$$\boldsymbol{F}_{\mathrm{in}} = \boldsymbol{I} + \left[g det\boldsymbol{F} \frac{\left(n_{\mathrm{ed}} - n_{\mathrm{ed}}^0 \right)}{V} \right] \boldsymbol{g} \otimes \boldsymbol{g} \qquad \mathrm{in}\, \Omega_{\mathrm{a}} \times \left[0, t^{\mathrm{end}} \right], \tag{23}$$

with the amount of substance of lithium $n_{\mathrm{ed}} = \int_{\Omega_{\mathrm{ed}}} c_{\mathrm{ed}}\, \mathrm{d}V$ and the associated amount of substance of lithium at the beginning of the simulation n_{ed}^0. Additionally, the vector $\boldsymbol{g}$ that identifies the spatial direction of the volume change and the current volume V are required. By a meaningful parameterization of the growth factor $g = \frac{M_{\mathrm{Li}}}{\rho_{\mathrm{Li}}}$ the cycling related volume change of the lithium metal anode is modeled. Hereby the molar mass of lithium is symbolized by M_{Li} and its mass density by ρ_{Li}.

2.4. Interface conditions

In this section we focus on the mathematical formulation of the electrode-electrolyte interface $\Gamma_{\mathrm{ed,el}} = \Gamma_{\mathrm{a,el}} \cup \Gamma_{\mathrm{c,el}}$, as well as on the interfaces between the (composite) electrodes and their adjacent current collectors $\Gamma_{\mathrm{cc,ed}} = \Gamma_{\mathrm{cc,a}} \cup \Gamma_{\mathrm{cc,c}} \cup \Gamma_{\mathrm{cc,el}}$ as depicted in Fig. 1.

For the mechanical problem we assume within this work that the different domains of the battery cannot separate or move relative to each other. Certainly, this is a simplification of reality as a separation of active material and solid electrolyte phases has been reported e.g. in [4]. Although with the present approach such effects are not spatially resolved, the battery cell can already be examined for areas where delamination could occur, since the mechanical stress state is available inside the whole computational domain. In the following we denote the interface where two or three bodies are in contact with $\Gamma_{\mathrm{c}} = \Gamma_{\mathrm{ed,el}} \cup \Gamma_{\mathrm{cc,ed}}$. The applied kinematic constraint when two bodies $\Omega^{(1)}$ and $\Omega^{(2)}$ are in contact then reads:

$$\boldsymbol{u}_{\mathrm{def}}^{(1)} = \boldsymbol{u}_{\mathrm{def}}^{(2)} \qquad \mathrm{on}\, \Gamma_{\mathrm{c}} \times \left[0, t^{\mathrm{end}} \right], \tag{24}$$

meaning that the displacements $\boldsymbol{u}_{\mathrm{def}}$ of both bodies have to match at their common interface. An extension to more than two sub-
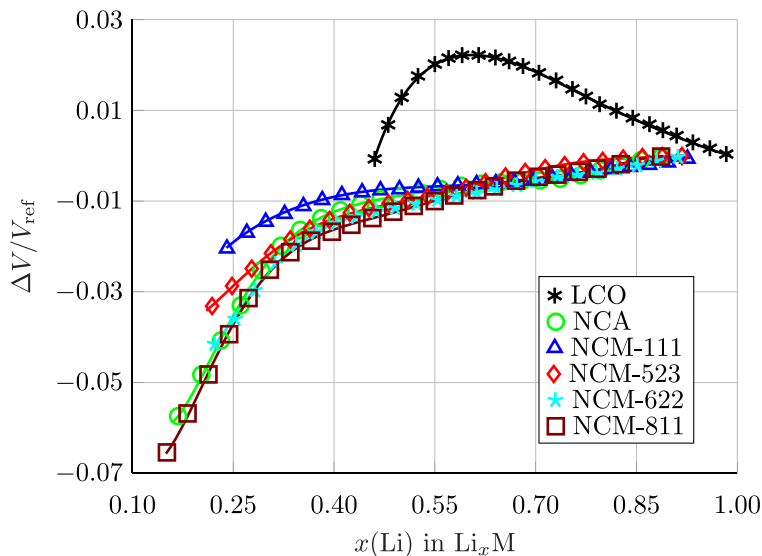

Fig. 2. Approximation of measured data as published in [5] (symbols) by a polynomial fit of order seven (solid lines).

domains is straightforward and mostly technical, even if so-called cross-points, where more than two bodies meet, appear.

For the electrochemical field, the conservation of lithium mass and charge has to be fulfilled at the electrode-electrolyte interface $\Gamma_{\text{ed,el}}$. To do so, we enforce the following constraints:

$$\boldsymbol{j}_{\text{ed}} \cdot \boldsymbol{n}_{\text{ed,el}} = \frac{1}{F} \boldsymbol{i}_{\text{ed}} \cdot \boldsymbol{n}_{\text{ed,el}} = \frac{1}{F} i = \frac{1}{F} \boldsymbol{i}_{\text{el}} \cdot \boldsymbol{n}_{\text{ed,el}} = \boldsymbol{j}_{\text{el}} \cdot \boldsymbol{n}_{\text{ed,el}} \qquad \text{on} \, \Gamma_{\text{ed,el}} \times \left[0, t^{\text{end}}\right], \tag{25}$$

with the lithium mass flux density and the electric current density in the electrodes being denoted by $\boldsymbol{j}_{\text{ed}} = -D\nabla c$ and $\boldsymbol{i}_{\text{ed}}$ (see Eq. (8)), respectively. At the electrolyte side, the lithium-ion mass flux density is represented by $\boldsymbol{j}_{\text{el}} = \frac{t_{\text{el}}}{F} \boldsymbol{i}_{\text{el}}$, where again the lithium-ion transference number t_{el} can be assumed to be close to unity [52,53] within the solid electrolytes investigated in this work. Furthermore, the corresponding electric current density inside the electrolyte is denoted by $\boldsymbol{i}_{\text{el}}$ (refer to Eq. (13)), and $\boldsymbol{n}_{\text{ed,el}}$ depicts the normal pointing from the electrode to the electrolyte domain. Moreover, i represents the current density at the interface, that is modeled using a Butler–Volmer formulation, as e.g. thermodynamically consistently derived in [57]:

$$i = i_0 \left[exp\left(\frac{\alpha_{\text{a}} F \eta}{RT}\right) - exp\left(-\frac{(1 - \alpha_{\text{a}}) F \eta}{RT}\right) \right], \tag{26}$$

with a so-called exchange current density i_0 and the anodic symmetry coefficient α_{a}. In contrast to the formulation in [57] we neglect the concentration dependence of the exchange current density in this paper. However, it should be noted that an incorporation of the thermodynamically consistently derived exchange current density is straightforward but not shown here for brevity. The overpotential η represents the driving force of the (de-)intercalation reaction at the interface of the active material and the solid electrolyte. It is modeled as follows:

$$\eta = \Phi_{\text{ed}} - \Phi_{\text{el}} - \Phi_0, \tag{27}$$

with the electric potential at the electrode and electrolyte side Φ_{ed} and Φ_{el}, respectively as well as the half cell open circuit potential (OCP) measured against pure lithium Φ_0. There are several approaches to model the OCP in literature, but we are not discussing this in detail here and are instead referring to [58]. At the anode side interface the OCP is set to zero $\left(\Phi_0 = 0 \, \text{on} \, \Gamma_{\text{a,el}}\right)$, as the OCP of the lithium metal anode is referenced against lithium.

Lastly, we need to describe the electrochemical interface conditions between the (composite) electrodes and their current collectors. The current collectors are modeled to be impermeable to lithium(-ions) resulting in the constraint that the mass flux across this interface has to vanish:

$$\boldsymbol{j}_{\text{ed}} \cdot \boldsymbol{n}_{\text{ed,cc}} = 0 = \boldsymbol{j}_{\text{el}} \cdot \boldsymbol{n}_{\text{el,cc}} \qquad \text{on} \, \Gamma_{\text{cc,ed}} \times \left[0, t^{\text{end}}\right], \tag{28}$$

where $\boldsymbol{n}_{\text{ed,cc}}$ and $\boldsymbol{n}_{\text{el,cc}}$ denote the normal pointing form the electrodes to the adjacent current collector and the normal pointing from the electrolyte to the corresponding current collector, respectively. As the electrolyte is an electrical insulator, meaning there is no flux of electrons across the electrolyte current collector interface, and there is no flux of ions across this interface either (cf. Eq. (28)), we can state that:

$$\boldsymbol{i}_{\text{el}} \cdot \boldsymbol{n}_{\text{el,cc}} = 0 \qquad \text{on} \, \Gamma_{\text{cc,el}} \times \left[0, t^{\text{end}}\right]. \tag{29}$$

Finally, we model the flux of electrons across the interface between the electrode and their current collector by applying an additional contact resistance R_{contact}. The interface equation thus reads:

$$\boldsymbol{i}_{\text{ed}} \cdot \boldsymbol{n}_{\text{ed,cc}} = \frac{\Phi_{\text{ed}} - \Phi_{\text{cc}}}{R_{\text{contact}}} \qquad \text{on} \, \Gamma_{\text{cc,ed}} \times \left[0, t^{\text{end}}\right], \tag{30}$$

with Φ_{cc} symbolizing the electric potential at the current collector side of the interface.

2.5. Boundary and initial conditions

Suitable boundary and initial conditions have to be applied to both fields of interest. As already mentioned before, we only consider a representative section in lateral direction from the real cell and therefore have to apply symmetry conditions to the corresponding surfaces. For the electrochemistry field this results in neither mass nor charge flux across these boundaries:

$$\boldsymbol{j} \cdot \boldsymbol{n} = 0 \qquad \text{on} \, \Gamma_{\text{cut}} \times \left[0, t^{\text{end}}\right], \tag{31}$$

$$\boldsymbol{i} \cdot \boldsymbol{n} = 0 \, \text{on} \, \Gamma_{\text{cut}} \times \left[0, t^{\text{end}}\right]. \tag{32}$$

In addition, as the current collectors are impermeable to lithium or lithium-ions (cf. Eq. (28)), there is also no mass flux across the outer boundaries of the current collectors:

$$\boldsymbol{j} \cdot \boldsymbol{n} = 0 \qquad \text{on} \left(\Gamma_{\text{cc,a-o}} \cup \Gamma_{\text{cc,c-o}}\right) \times \left[0, t^{\text{end}}\right]. \tag{33}$$

Moreover, the electric potential is set to a reference value at the outer boundary of the anode side current collector:

$$\Phi = 0 \qquad \text{on} \, \Gamma_{\text{cc,a-o}} \times \left[0, t^{\text{end}}\right]. \tag{34}$$

To enable galvanostatic charging of the cell, we impose an electric current density $\widehat{i}$ normal to the outer boundary of the cathode side current collector:

$$-\boldsymbol{i} \cdot \boldsymbol{n} = \widehat{i} \qquad \text{on} \, \Gamma_{\text{cc,c-o}} \times \left[0, t^{\text{end}}\right]. \tag{35}$$

At the beginning, the electrochemical state of the cell is assumed to be in static equilibrium:

$$c = c_{\text{ed}}^0 \qquad \text{in} \, \Omega_{\text{ed}} \times \{0\}, \tag{36}$$

$$c = c_{\text{el}}^0 \, \text{in} \, \Omega_{\text{el}} \times \{0\}, \tag{37}$$

with a prescribed value of the initial lithium(-ion) concentration within the electrodes c_{ed}^0 and the electrolyte c_{el}^0. Initial conditions for the electric potential fields Φ_{ed} and Φ_{el} are not required, as Eqs. (9) and (14) for the conservation of charge are stationary.

For the solid mechanics field we also need to impose proper initial and boundary conditions as follows:

$$\boldsymbol{u}_{\text{def}} = \widehat{\boldsymbol{u}} \qquad \text{on} \, \Gamma_u \times \left[0, t^{\text{end}}\right], \tag{38}$$

$$(\boldsymbol{F} \cdot \boldsymbol{S}) \cdot \boldsymbol{N} = \widehat{\boldsymbol{t}} \, \text{on} \, \Gamma_\sigma \times \left[0, t^{\text{end}}\right], \tag{39}$$

$$\boldsymbol{u}_{\text{def}} = \boldsymbol{u}_0 \, \text{in} \, \Omega \times \{0\}, \tag{40}$$

$$\dot{\boldsymbol{u}}_{\text{def}} = \dot{\boldsymbol{u}}_0 \, \text{in} \, \Omega \times \{0\}, \tag{41}$$

with the fixed values $\widehat{\boldsymbol{u}}$ and $\widehat{\boldsymbol{t}}$ for the Dirichlet and Neumann boundary conditions, respectively. Moreover, the initial values for the displacements $\boldsymbol{u}_0$, and the velocities $\dot{\boldsymbol{u}}_0$ are given. In order to be in line with the aforementioned boundary conditions for the electrochemical field, we also have to apply symmetry conditions in lateral direction, meaning that the normal displacement at the lateral sides is set to zero using a Dirichlet boundary condition. In addition, the derivative of the displacements in normal direction has to vanish at those surfaces to ensure symmetry.

3. Aspects of the numerical model

The continuous modeling equations as presented in Section 2 are solved using the finite element method whose main steps are shown below exemplarily. Finally, we will also discuss the basics of the monolithic solution approach chosen to solve this highly non-linear coupled problem.

3.1. Finite element formulation

The finite element method is based on the weak form of the modeling equations. Thus, the weak form of the equations has to be derived and discretized in time and space. For time integration, we apply the well-known one-step-theta method.

3.1.1. Weak form

In the following we base our formulation on the *principle of virtual work*. The virtual energy of the coupled problem calculates as follows:

$$\delta W = \delta W_{\text{elch}} + \delta W_{\text{mech}} + \delta W_{\text{constr}} = 0, \tag{42}$$

with δW_{elch} and δW_{mech} denoting the contributions of the electrochemical and solid mechanics fields, respectively. Moreover, δW_{constr} represents the energy contribution due to interface constraints. As solution and test function spaces we apply:

$$\mathscr{S}_c = \left\{c \in H^1(\Omega)\right\} \mathscr{T}_c = \left\{\delta g \in H^1(\Omega)\right\}, \tag{43}$$

$$\mathscr{S}_\Phi = \left\{\Phi \in H^1(\Omega)\right\} \mathscr{T}_\Phi = \left\{\delta\Phi \in H^1(\Omega) \, \bigm| \, \delta\Phi = 0 \quad \text{on} \quad \Gamma_{\text{cc,a-o}}\right\}, \tag{44}$$

$$\mathscr{S}_{\boldsymbol{u}_{\text{def}}} = \left\{\boldsymbol{u}_{\text{def}} \in H^1(\Omega)\right\} \qquad \mathscr{T}_{\boldsymbol{u}_{\text{def}}} = \left\{\delta\boldsymbol{u}_{\text{def}} \in H^1(\Omega) \, \bigm| \, \delta\boldsymbol{u}_{\text{def}} = 0 \quad \text{on} \quad \Gamma_u\right\}, \tag{45}$$

with the usual Sobolev spaces $H^1(\Omega)$ of square-integrable functions with weak first derivative defined on the respective domains as presented in Fig. 1.

Since the procedure from continuous strong form to fully discretized weak form is conceptually identical for most of the presented modeling equations, it is only shown for two exemplary equations in the following. Namely, the mass conservation Eq. (20) within the

electrode and the treatment of the interface constraint, the so-called mesh tying, including the condensation of Lagrange multipliers.

By multiplication with an arbitrary test function δg from the admissible test function space $\mathcal{T}_c$ and an integration over the relevant domain, the virtual work contribution of the mass conservation Eq. (20) in the electrode is obtained. Integration by parts, and the exploitation of the homogeneous Neumann boundary conditions from Eqs. (28) and (31) result in the corresponding weak form:

$$\delta W_{\mathrm{elch,c,ed}} = \int_{\Omega_{\mathrm{ed}}} \delta g \left. \frac{\partial c}{\partial t} \right|_X \mathrm{d}\Omega + \int_{\Omega_{\mathrm{ed}}} \delta g \, c \nabla \cdot \dot{\boldsymbol{u}}_{\mathrm{def}} \, \mathrm{d}\Omega + \int_{\Omega_{\mathrm{ed}}} \nabla \delta g \cdot D \, \nabla c \, \mathrm{d}\Omega + \int_{\Gamma_{\mathrm{ed,el}}} \delta g \boldsymbol{j}_{\mathrm{ed}} \cdot \boldsymbol{n} \, \mathrm{d}\Gamma = 0, \tag{46}$$

where we additionally substituted $\boldsymbol{j}_{\mathrm{ed}} = -D\nabla c$ into the last term. By an interpretation of δg as a virtual molar free energy flux this expression represents the virtual work within the electrodes $\delta W_{\mathrm{elch,c,ed}}$, being one component of δW_{elch} in Eq. (42).

The interface constraint between the electrodes and the electrolyte for the electrochemical field as formulated in Eq. (25) is taken into account in the last term of Eq. (46). In our previous work in the context of conventional lithium-ion batteries [59], we showed that such a constraint can be introduced by either direct insertion into the weak form, or by constraint enforcement using Lagrangian multipliers with no difference in accuracy or robustness. In this work we decided to directly insert the interface constraint. An equivalent procedure is performed for the weak form of the mass conservation of the electrolyte as well as for the weak form of the charge conservation inside the electrodes and the electrolytes.

To introduce the mechanical interface constraint into the system, we first generalize Eq. (24) to n contacting bodies at the interface Γ_c. Therefore, we arbitrarily choose one of those bodies to be the so-called *master* body and the remaining $n - 1$ bodies to be *slave* bodies indicated by the indices "m" and "s", respectively. The reformulation into the weak form leads to the following expression of the work contribution due to mechanical interface constraints:

$$W_{\mathrm{constr}} = \sum_{j=1}^{n-1} \int_{\Gamma_c} \left(\boldsymbol{\lambda}^{j\mathrm{T}} \left(\boldsymbol{u}_{\mathrm{def,m}} - \boldsymbol{u}_{\mathrm{def,s}}^j \right) \right) \mathrm{d}\Gamma. \tag{47}$$

The test functions $\boldsymbol{\lambda}^j$ can be interpreted as forces that have to be applied to the bodies required to fulfill the interface constraint. Variation of this equation returns the contribution to the virtual work as follows:

$$\delta W_{\mathrm{constr}} = \sum_{j=1}^{n-1} \left[\int_{\Gamma_c} \left(\delta \boldsymbol{\lambda}^{j\mathrm{T}} \left(\boldsymbol{u}_{\mathrm{def,m}} - \boldsymbol{u}_{\mathrm{def,s}}^j \right) + \left(\delta \boldsymbol{u}_{\mathrm{def,m}} - \delta \boldsymbol{u}_{\mathrm{def,s}}^j \right)^{\mathrm{T}} \boldsymbol{\lambda}^j \right) \mathrm{d}\Gamma \right]. \tag{48}$$

3.1.2. Discretization in time

For the discretization in time, the time interval of interest is split into coherent, non-overlapping, and not necessarily uniform time intervals Δt. The nth time interval is then defined to start at time t^n and to end at time t^{n+1}, where the semi-discrete values of the primary variables at time t^j are denoted by the superscript $*^j$. By applying the one-step-theta method to Eq. (46) we obtain:

$$\int_{\Omega_{\mathrm{ed}}} \delta g \, \frac{c^{n+1} - c^n}{\Delta t} \, \mathrm{d}\Omega + \int_{\Omega_{\mathrm{ed}}} \delta g \, c^{n+\theta} \, \nabla \cdot \dot{\boldsymbol{u}}^{n+\theta} \, \mathrm{d}\Omega + \int_{\Omega_{\mathrm{ed}}} \nabla \delta g \cdot D \, \nabla c^{n+\theta} \, \mathrm{d}\Omega + \int_{\Gamma_{\mathrm{ed,el}}} \delta g \boldsymbol{j}_{\mathrm{ed}}^{n+\theta} \cdot \boldsymbol{n}^{n+\theta} \, \mathrm{d}\Gamma = 0, \tag{49}$$

where $\theta \in [0; 1]$ is the one-step-theta parameter, and for an arbitrary scalar- or vector-valued quantity $*$ the following relation holds:

$$*^{n+\theta} = \theta *^{n+1} + (1 - \theta) *^n. \tag{50}$$

Since Eq. (48) is stationary the time integration procedure is trivial and therefore not shown here.

Throughout this paper we set $\theta = 0.5$ resulting in the Crank–Nicolson method which is second-order accurate in time.

3.1.3. Discretization in space

Finally, the system is discretized in space by subdividing the whole computational domain Ω into non-overlapping finite elements building up its discrete counterpart indicated by $*^{\mathrm{h}}$. The integration over the complete domain is consequently split up into a sum over all finite elements and an integration over the respective elements. For Eq. (49) this procedure is exemplary shown below:

$$\sum_{i=1}^{n_{\mathrm{ele,ed}}} \left(\int_{\Omega_{\mathrm{ed}}^{\mathrm{h},i}} \delta g \, \frac{c^{n+1} - c^n}{\Delta t} \, \mathrm{d}\Omega + \int_{\Omega_{\mathrm{ed}}^{\mathrm{h},i}} \delta g \, c^{n+\theta} \, \nabla \cdot \dot{\boldsymbol{u}}^{n+\theta} \, \mathrm{d}\Omega + \int_{\Omega_{\mathrm{ed}}^{\mathrm{h},i}} \nabla \delta g \cdot D \, \nabla c^{n+\theta} \, \mathrm{d}\Omega + \int_{\Gamma_{\mathrm{ed,el}}^{\mathrm{h},i}} \delta g \boldsymbol{j}_{\mathrm{ed}}^{n+\theta} \cdot \boldsymbol{n}^{n+\theta} \, \mathrm{d}\Gamma \right) = 0, \tag{51}$$

with $\boldsymbol{j}_{\mathrm{ed}}^{n+\theta} = \mathrm{fn}\left(c^{n+\theta}, \phi^{n+\theta}\right)$, and $n_{\mathrm{ele,ed}}$ denoting the number of finite elements the discretized electrode domain consists of. Please note, that in the presented work the electrochemical and solid mechanics fields are identically discretized in space, even though their discretizations could also be independent of each other. Furthermore, the solution and test function spaces are restricted to the corresponding finite-dimensional sub spaces consisting of Lagrange polynomials with an isoparametric interpolation. The finite element approximation of a generic quantity ζ at time t^{n+1} can thus be written as:

$$\boldsymbol{\zeta}^{\mathrm{h},n+1} = \sum_{i=1}^{n_{\mathrm{nodes}}} N_{\zeta,i}^{\mathrm{h}} \overline{\zeta}_i^{n+1} = N_{\zeta}^{\mathrm{h}} \overline{\boldsymbol{\zeta}}^{n+1}, \tag{52}$$

with n_{nodes} denoting the number of nodes of the finite element discretization, the Lagrange polynomial $N_{\zeta,i}^{\text{h}}$ taken from the corresponding discrete solution $\mathscr{S}_{\zeta}^{\text{h}}$ or test function space $\mathscr{T}_{\zeta}^{\text{h}}$ associated with node i, and the discrete nodal values depicted as $\overline{\zeta}_i$.

Applying this procedure to all presented modeling equations results in a discrete system of non-linear equations of the following form:

$$
\begin{pmatrix}
\boldsymbol{R}_{\boldsymbol{u}_{\text{def}}}^{n+1}\left(\overline{\boldsymbol{u}}_{\text{def}}^{n+1}, \overline{\boldsymbol{\lambda}}^{n+1}, \overline{\boldsymbol{c}}^{n+1}, \overline{\boldsymbol{\Phi}}^{n+1}\right) \\
\boldsymbol{R}_{\lambda}^{n+1}\left(\overline{\boldsymbol{u}}_{\text{def}}^{n+1}, \overline{\boldsymbol{\lambda}}^{n+1}, \overline{\boldsymbol{c}}^{n+1}, \overline{\boldsymbol{\Phi}}^{n+1}\right) \\
\boldsymbol{R}_{c}^{n+1}\left(\overline{\boldsymbol{u}}_{\text{def}}^{n+1}, \overline{\boldsymbol{\lambda}}^{n+1}, \overline{\boldsymbol{c}}^{n+1}, \overline{\boldsymbol{\Phi}}^{n+1}\right) \\
\boldsymbol{R}_{\Phi}^{n+1}\left(\overline{\boldsymbol{u}}_{\text{def}}^{n+1}, \overline{\boldsymbol{\lambda}}^{n+1}, \overline{\boldsymbol{c}}^{n+1}, \overline{\boldsymbol{\Phi}}^{n+1}\right)
\end{pmatrix}
=
\begin{pmatrix}
\boldsymbol{0} \\
\boldsymbol{0} \\
\boldsymbol{0} \\
\boldsymbol{0}
\end{pmatrix},
\tag{53}
$$

where $\boldsymbol{R}_{\boldsymbol{u}_{\text{def}}}^{n+1}, \boldsymbol{R}_{\lambda}^{n+1}, \boldsymbol{R}_{c}^{n+1}, \boldsymbol{R}_{\Phi}^{n+1}$ are the discrete residual vectors representing the solid mechanics, mechanical interface constraint, mass conservation, and charge conservation equations, respectively. The residual vectors depend on the discrete solution vectors $\overline{\boldsymbol{u}}_{\text{def}}^{n+1}, \overline{\boldsymbol{\lambda}}^{n+1}$, $\overline{\boldsymbol{c}}^{n+1}, \overline{\boldsymbol{\Phi}}^{n+1}$ at the most recent time t^{n+1}.

3.2. Linearization of the non-linear system of equations and monolithic solution approach

Our long experience in dealing with coupled multi-field problems has often shown superior robustness and frequently also enhanced efficiency of monolithic compared to partitioned schemes, like for example in the context of fluid–structure interaction [60], thermo-structure interaction [61], electro-chemo-thermal problems [44], or general n-field coupled problems [62]. Thus, we decided to treat the system at hand in a monolithic fashion. To linearize the highly non-linear system of discrete equations we apply the Newton–Raphson method and solve for the nodal unknowns in an iterative manner. In every Newton–Raphson iteration step j the following sparse linear system of equations arises:

$$
\begin{pmatrix}
\dfrac{\partial \boldsymbol{R}_{\boldsymbol{u}_{\text{def}}}^{n+1}}{\partial \overline{\boldsymbol{u}}_{\text{def}}^{n+1}} & \dfrac{\partial \boldsymbol{R}_{\boldsymbol{u}_{\text{def}}}^{n+1}}{\partial \overline{\boldsymbol{\lambda}}^{n+1}} & \dfrac{\partial \boldsymbol{R}_{\boldsymbol{u}_{\text{def}}}^{n+1}}{\partial \overline{\boldsymbol{c}}^{n+1}} & \dfrac{\partial \boldsymbol{R}_{\boldsymbol{u}_{\text{def}}}^{n+1}}{\partial \overline{\boldsymbol{\Phi}}^{n+1}} \\[2ex]
\dfrac{\partial \boldsymbol{R}_{\lambda}^{n+1}}{\partial \overline{\boldsymbol{u}}_{\text{def}}^{n+1}} & \dfrac{\partial \boldsymbol{R}_{\lambda}^{n+1}}{\partial \overline{\boldsymbol{\lambda}}^{n+1}} & \dfrac{\partial \boldsymbol{R}_{\lambda}^{n+1}}{\partial \overline{\boldsymbol{c}}^{n+1}} & \dfrac{\partial \boldsymbol{R}_{\lambda}^{n+1}}{\partial \overline{\boldsymbol{\Phi}}^{n+1}} \\[2ex]
\dfrac{\partial \boldsymbol{R}_{c}^{n+1}}{\partial \overline{\boldsymbol{u}}_{\text{def}}^{n+1}} & \dfrac{\partial \boldsymbol{R}_{c}^{n+1}}{\partial \overline{\boldsymbol{\lambda}}^{n+1}} & \dfrac{\partial \boldsymbol{R}_{c}^{n+1}}{\partial \overline{\boldsymbol{c}}^{n+1}} & \dfrac{\partial \boldsymbol{R}_{c}^{n+1}}{\partial \overline{\boldsymbol{\Phi}}^{n+1}} \\[2ex]
\dfrac{\partial \boldsymbol{R}_{\Phi}^{n+1}}{\partial \overline{\boldsymbol{u}}_{\text{def}}^{n+1}} & \dfrac{\partial \boldsymbol{R}_{\Phi}^{n+1}}{\partial \overline{\boldsymbol{\lambda}}^{n+1}} & \dfrac{\partial \boldsymbol{R}_{\Phi}^{n+1}}{\partial \overline{\boldsymbol{c}}^{n+1}} & \dfrac{\partial \boldsymbol{R}_{\Phi}^{n+1}}{\partial \overline{\boldsymbol{\Phi}}^{n+1}}
\end{pmatrix}_{j}
\cdot
\begin{pmatrix}
\Delta \overline{\boldsymbol{u}}_{\text{def}}^{n+1} \\
\Delta \overline{\boldsymbol{\lambda}}^{n+1} \\
\Delta \overline{\boldsymbol{c}}^{n+1} \\
\Delta \overline{\boldsymbol{\Phi}}^{n+1}
\end{pmatrix}_{j+1}
= -
\begin{pmatrix}
\boldsymbol{R}_{\boldsymbol{u}_{\text{def}}}^{n+1} \\
\boldsymbol{R}_{\lambda}^{n+1} \\
\boldsymbol{R}_{c}^{n+1} \\
\boldsymbol{R}_{\Phi}^{n+1}
\end{pmatrix}_{j},
\tag{54}
$$

where the increment vector is used to iteratively update the nodal unknowns from Newton–Raphson iteration step j to $j+1$ until the L^2-norm of the residual is smaller than a predefined value as follows:

$$
\begin{pmatrix}
\overline{\boldsymbol{u}}_{\text{def}}^{n+1} \\
\overline{\boldsymbol{\lambda}}^{n+1} \\
\overline{\boldsymbol{c}}^{n+1} \\
\overline{\boldsymbol{\Phi}}^{n+1}
\end{pmatrix}_{j+1}
=
\begin{pmatrix}
\Delta \overline{\boldsymbol{u}}_{\text{def}}^{n+1} \\
\Delta \overline{\boldsymbol{\lambda}}^{n+1} \\
\Delta \overline{\boldsymbol{c}}^{n+1} \\
\Delta \overline{\boldsymbol{\Phi}}^{n+1}
\end{pmatrix}_{j+1}
+
\begin{pmatrix}
\overline{\boldsymbol{u}}_{\text{def}}^{n+1} \\
\overline{\boldsymbol{\lambda}}^{n+1} \\
\overline{\boldsymbol{c}}^{n+1} \\
\overline{\boldsymbol{\Phi}}^{n+1}
\end{pmatrix}_{j}.
\tag{55}
$$

The next step is to condense the Lagrange multipliers and the displacements on the surface of the slave body from the linear system shown above. Therefore, we subdivide the complete displacement vector $\overline{\boldsymbol{u}}_{\text{def}}^{n+1} = \overline{\boldsymbol{u}}_{\text{def,i,m,s}}^{n+1} = \left[\overline{\boldsymbol{u}}_{\text{def,i}}^{n+1}, \overline{\boldsymbol{u}}_{\text{def,m}}^{n+1}, \overline{\boldsymbol{u}}_{\text{def,s}}^{n+1}\right]^{\text{T}}$ into degrees of freedom from the interior of the bodies, the surface of the master body, and the surfaces of the slave bodies denoted by the indices "i", "m", and "s", respectively. Details on the condensation procedure can be found in Appendix D. The linear system resulting from this procedure is the final system to be solved featuring the following 3x3 block structure:

$$
\left(
\begin{array}{ccc}
\dfrac{\partial \boldsymbol{R}^{n+1}_{u_{\text{def,i,m}}}}{\partial \overline{\boldsymbol{u}}^{n+1}_{\text{def,i,m}}} & \dfrac{\partial \boldsymbol{R}^{n+1}_{u_{\text{def,i,m}}}}{\partial \overline{\boldsymbol{c}}^{n+1}} & \dfrac{\partial \boldsymbol{R}^{n+1}_{u_{\text{def,i,m}}}}{\partial \overline{\boldsymbol{\Phi}}^{n+1}} \\[3mm]
\dfrac{\partial \boldsymbol{R}^{n+1}_{c}}{\partial \overline{\boldsymbol{u}}^{n+1}_{\text{def,i,m}}} & \dfrac{\partial \boldsymbol{R}^{n+1}_{c}}{\partial \overline{\boldsymbol{c}}^{n+1}} & \dfrac{\partial \boldsymbol{R}^{n+1}_{c}}{\partial \overline{\boldsymbol{\Phi}}^{n+1}} \\[3mm]
\dfrac{\partial \boldsymbol{R}^{n+1}_{\Phi}}{\partial \overline{\boldsymbol{u}}^{n+1}_{\text{def,i,m}}} & \dfrac{\partial \boldsymbol{R}^{n+1}_{\Phi}}{\partial \overline{\boldsymbol{c}}^{n+1}} & \dfrac{\partial \boldsymbol{R}^{n+1}_{\Phi}}{\partial \overline{\boldsymbol{\Phi}}^{n+1}}
\end{array}
\right)\Bigg|_{j}
\cdot
\left(
\begin{array}{c}
\Delta \overline{\boldsymbol{u}}^{n+1}_{\text{def,i,m}} \\[2mm]
\Delta \overline{\boldsymbol{c}}^{n+1} \\[2mm]
\Delta \overline{\boldsymbol{\Phi}}^{n+1}
\end{array}
\right)\Bigg|_{j+1}
= -
\left(
\begin{array}{c}
\boldsymbol{R}^{n+1}_{u_{\text{def,i,m}}} \\[2mm]
\boldsymbol{R}^{n+1}_{c} \\[2mm]
\boldsymbol{R}^{n+1}_{\Phi}
\end{array}
\right)\Bigg|_{j}.
\tag{56}
$$

Especially for realistic problem scenarios those linear systems consist of up to some millions of degrees of freedom rendering direct solvers unfavorable due to their larger memory consumption and arithmetic complexity compared to iterative solvers. However, since different physical fields are covered, and coupling matrices are introduced as off-diagonal blocks of the matrix due to the monolithic solution approach, the resulting system matrix is usually ill-conditioned. Thus, also an application of standard iterative solvers is not possible. To circumvent this issue we extend the physics-based preconditioning approach developed for conventional lithium-ion batteries in [44] to be applicable to the presented modeling approach. It combines a block Gauss–Seidel method with an algebraic multi-grid approach to enable flexible preconditioning based on both physical and geometric information. This approach allows the nonlinear complex ASSB model presented in this paper to be applied to realistic problem scenarios as exemplary depicted in Fig. 3.

4. Numerical examples

The proposed numerical ASSB model is now applied to different scenarios to both verify the model and derive insights into this coupled problem that go beyond those from experimental studies. All simulations are carried out using our in-house multi-physics research code BACI [63] in which we implemented the presented ASSB model. To visualize the geometries and physical fields we employ Kitware ParaView 5.5.2 [64]. Moreover, MATLAB R2020b [65] is used to generate the plots.

4.1. Setup of the numerical examples

In the following the three different computational domains used to compute the results are described. Furthermore, the applied material setup as well as the initial and boundary conditions to represent the investigated operating scenarios are detailed on.

4.1.1. Definition of different computational domains

Within this publication three different computational domains are investigated. The first one (cf. Fig. 3) is based on geometric data of a real ASSB cell as described in [18] and therefore hereinafter called "realistic geometry". From left to right, it consists of the anode side current collector (orange), a lithium metal anode (gray), a solid electrolyte (green), the cathode active material particles (anthracite), and the cathode side current collector (light gray). The overall dimensions of this setup are listed in Table B.5 in the appendix. Coreform Cubit 2021.3 [66] is used to generate this computational domain and perform the meshing procedure. The resulting finite element mesh consists of 276,533 nodes defining $1,343,275$ tetrahedral elements with linear shape functions and resulting in about 1.3 million degrees of freedom. This finite element mesh is used to show the applicability of the proposed model to real-world scenarios, and to benchmark against results presented in the aforementioned publication [18]. A geometric analysis of the conductively connected parts of the composite cathode active material shows that the total volume is divided into six non-interconnected parts whose volume shares in the total volume vary between 96.7% and 0.08%.

Computational domain two and three are geometrically reduced versions of the previously described configuration and are shown in Fig. 4. Subsequently, they are referred to as "simplified geometry". Based on those domains the verification of the presented model is carried out. Moreover, the importance to include the current collectors in ASSB simulations is discussed. Therefore, the left computational domain represents an ASSB cell including current collectors, whereas the right is the exact same cell but without current collectors. One main feature of those simplified geometries is the setup of the active material particles within the composite cathode. Based on the finding that the whole active material volume can be separated into different clusters for the realistic geometry described above, this is also reflected in the setup of the active material particles for the simplified geometries by a separation into two parts. In

Fig. 3. Realistic geometry of an ASSB battery cell based on geometric data from [18].

Table B.5 the dimensions of the setups are given. Again, the displayed finite element meshes are created using Coreform Cubit 2021.3 [66]. The spatial discretizations are based on tetrahedral elements with linear shape functions and consist of 3,138 nodes, and 2,430 nodes for the mesh with current collectors, and the mesh without current collectors, respectively.

Remark. In the absence of current collectors, also some equations presented in Section 2 have to be adapted accordingly. All equations that are defined on the current collector domains $\Omega_{cc,a}$ and $\Omega_{cc,c}$ are neglected. Moreover, the interface Eq. (24) is only defined on $\Gamma_{ed,el}$ and the interface Eq. (28)–(30) are replaced by the boundary Eq. (33)–(35), respectively.

4.1.2. Materials of the ASSB cells

Throughout this paper one material setup of the ASSB cells is used for all simulations. If current collectors are considered, they consist of copper at the anode side and of aluminum at the cathode side. The cathode active material is $Li_\chi Ni_{0.6}Mn_{0.2}Co_{0.2}O_2$ (NMC622). Finally, the setup is completed by a $\beta - Li_3PS_4$ ($\beta - LPS$) solid electrolyte separator and a lithium metal anode. All material parameters can be found in the appendix. The mechanical as well as electrochemical material parameters are listed in Tables B.2 and B.3, respectively. The parameterization of the inelastic deformation laws in Eqs. (22) and (23) is presented in Table B.1.

4.1.3. Initial and operating conditions

All simulations carried out in this work are started at a fully charged state. The initial conditions concerning the electrochemistry field are shown in Table B.4. For the solid mechanics field we assume that in the initial state we have both, vanishing displacements $u_0 = 0$, and vanishing deformation velocities $\dot{u}_0 = 0$. Moreover, the ASSB cells are discharged at different constant currents, representing C-rates of 0.1 or 0.5. A C-rate of x means that the battery is fully charged, or discharged within $\frac{1}{x}$ hours. Finally, the constant current discharge process is usually stopped at a lower cutoff voltage of 2.6 V. If not explicitly stated differently, the normal directions of all outer surfaces are constrained, i.e. they cannot move in normal direction as already described in Section 2.5.

4.2. Validation of the presented ASSB model

The validation of the presented ASSB model is performed in three steps. First we check the conservation of mass and charge on deforming meshes to validate that the model has been formulated and implemented consistently. Then we discuss the importance to include current collectors in ASSB simulations in order to deduce the recommended choice of the computational domains for the upcoming numerical investigations. Finally, the results of our ASSB model are compared to published electrochemical results from [18] to validate that our model is capable to reproduce those results.

4.2.1. Validation of the conservation of mass and charge

As the coupling of solid mechanics and electrochemistry is the main aspect of this paper we focus on the verification of the conservation of mass and charge on deforming meshes in this section. Since both conservation laws are not independent, it is sufficient to monitor the amount of substance of lithium within the anode and cathode, as well as the amount of substance of lithium-ions in the solid electrolyte. A constant current discharge at a C-rate of 0.5 until 2.6 V is applied to the simplified geometry including current collectors as already shown in Fig. 4. The resulting amount of substances in the different domains are visualized over time in Fig. 5. As expected for this operating scenario a linear decline in the amount of substance of lithium within the anode and a linear increase in the amount of substance of lithium within the cathode with the same absolute slope is obtained. Moreover, due to the conservation of charge, a constant amount of lithium-ions within the solid electrolyte throughout the discharge process is expected. This is displayed by the constant progression of the red graph. Consequently, the total amount of lithium and lithium-ions remains constant during the operation, as indicated by the black curve. The simulation shows that the conservation of mass is only violated by a very small relative deviation in the order of 10^{-5}%.

The slight error in the mass conservation equation originates from the highly non-linear nature of the respective Eq. (20) and (21). Due to the non-linearity, the discrete solution does not exactly fulfill the mass conservation as expected. However, we still need to prove that the formulation is consistent, i.e. that the error is decreasing for a refinement of the time step size. Therefore, we perform a temporal convergence study on the same problem setup as above, but varying the time step size from 5 s to 300 s. Furthermore, we modify the cutoff voltage to 3.65 V since the steep gradient in the open circuit potential (see Fig. B.1) for lower cutoff voltages cannot be resolved using such large time steps. As a guide to the eye we introduce the slopes for linear and quadratic convergence using dashed lines in Fig. 6.
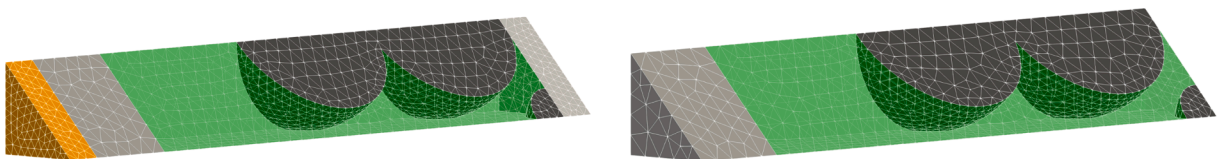
Fig. 4. Simplified geometries to evaluate the properties of our proposed model. Left: ASSB geometry including current collectors. Right: ASSB geometry without current collectors.
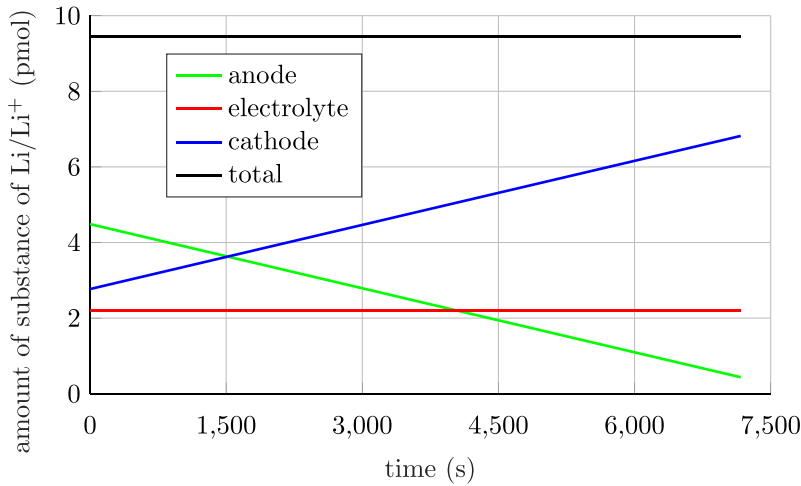
Fig. 5. Amount of substance of lithium and lithium-ions during constant current discharging at 0.5 C until 2.6 V is reached.

Since we employ the Crank–Nicolson method we expect the solution to be second-order accurate in time. The plot shows, that for very large time steps the convergence rate is slightly diminished. Whereas for smaller time steps even faster convergence than expected is obtained. For the investigated time interval the averaged convergence rate is a bit faster than the expected quadratic convergence. Thus, we were able to successfully show the consistent implementation of our model. To sum up, it is verified that both mass and charge conservation are indeed fulfilled by our proposed model.

4.2.2. Validation of the setup of the computational domain

A correct setup of the computational domain is also important to obtain physically reasonable results. To investigate this, we discuss the necessity to explicitly consider the current collectors in ASSB simulations. Therefore, the two simplified geometries as already shown in Fig. 4 are discharged using a constant current at a C-rate of 0.5. Fig. 7 shows the cell voltage progression over time during the discharge process. For the cell setup without current collectors, the cell potential almost immediately drops to the pre-scribed cutoff voltage of 2.6 V. It is already reached after only approximately 150 seconds of discharging. Opposed to this, the cell voltage curve for the ASSB cell explicitly including the current collectors exhibits a rather flat course, until at about 6,500 s a steep decline to the cutoff voltage of 2.6 V is visible. As expected, the curve shows a similar course as the open circuit potential reported by [67] (cf. Fig. B.1).

The origin of this observation can be revealed by comparing the state of charge (SoC) inside the separated volumes over time for the different cell setups (see Fig. 8 for a visualization of the volumes). For the setup without current collectors, we see an extreme difference in the SoC of the two different volumes in Fig. 8. When the cutoff voltage is reached, i.e. at the end of the simulation time, the small volume is already discharged until about 8% SoC, whereas the large volume still features more than 99% SoC. In combination with local concentration gradients inside the volumes due to the discharge process, the surface of the small volume is already
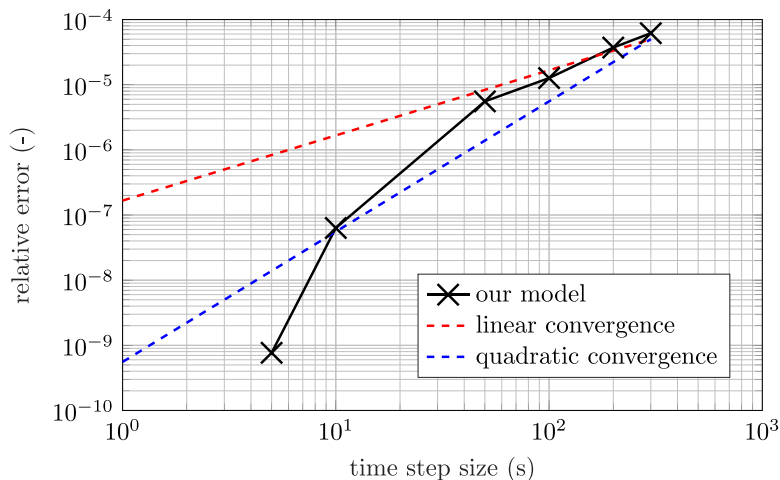
Fig. 6. Relative error in conservation of mass at the end of the simulation over time step size of the simulation.
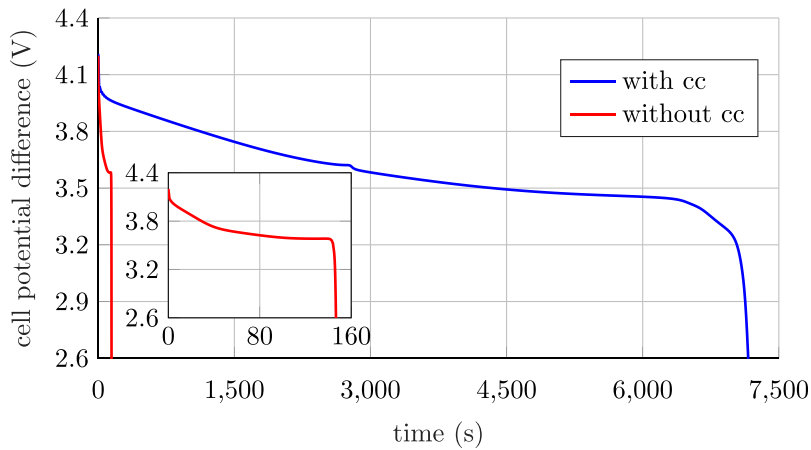
Fig. 7. Comparison of the cell potential differences over time during discharge for an ASSB cell with and without incorporation of current collectors (cc).

completely lithiated. Consequently, this volume has already reached the cutoff voltage and thereby dominates the charge–discharge behavior of the system. In contrast, for the setup including current collectors we see a less pronounced disbalance in SoC for the different volumes. The described phenomenon originates from the geometric setup of the composite cathodes in combination with its boundary conditions. When no current collectors are considered a uniform current density is applied to the surface $\Gamma_{cc,c}$ of all cathode particle clusters (see Fig. 1), such that particle clusters with small volume discharge faster than particle clusters with large volume. Opposed to that, in the simulation setup including current collectors the different SoC in the particle clusters results in varying potentials between the particle clusters due to the lithiation dependent open circuit potential. Different potentials within the active materials then lead to changed potential differences w.r.t. the potential of the current collector and thereby to an adapted flux between the current collector and the independent clusters of active materials. Finally, we can state that the incorporation of current collectors couples the volumes with intersection to the current collector and thereby enables a physical balancing of local fluxes between those volumes.

Furthermore, a kink in the cell voltage progression of the simulation including current collectors is apparent at around 2,900 s in Fig. 7. This can again be explained using Fig. 8 by exhibiting that the small volume is nearly completely discharged at around 2,900 s. After that it shows an almost horizontal progression until the end of the simulation, meaning that it does not take part in the discharge process anymore. The cell voltage curve in Fig. 7 reflects this behavior in the aforementioned kink. It originates from the fact that the open circuit potential has a very steep progression towards full lithiation (cf. Fig. B.1) and the smaller volume is already exhibiting those lithiation states.

Remark. We want to briefly discuss two further possibilities to tackle the described problem. Since clusters of connected particles can only occur on the composite electrode side, the first option would be to move the definition of the potential as shown in Eq. (34) to the
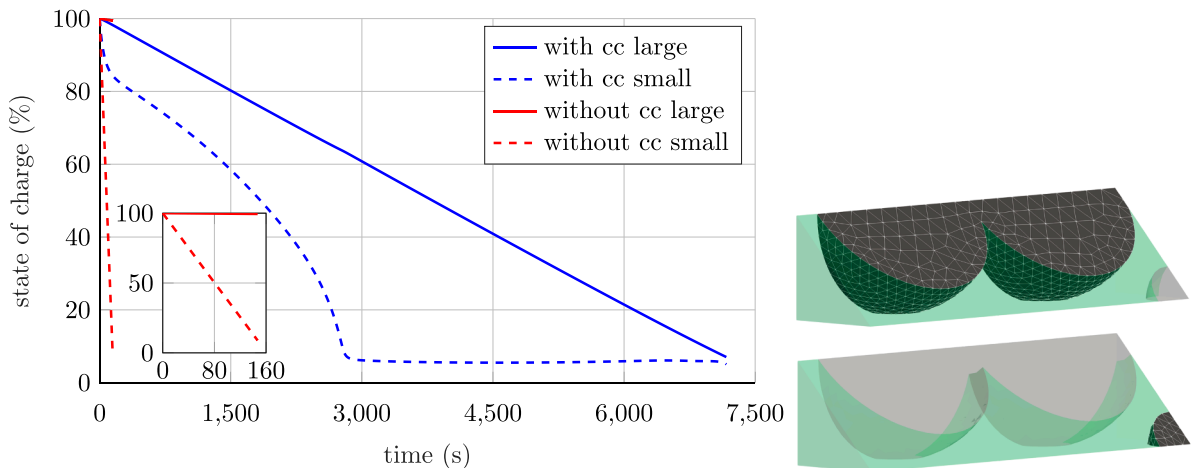
Fig. 8. Left: Comparison of the state of charge over time during discharge in the different cathode volumes (small/large) for an ASSB cell with and without incorporation of current collectors (cc). Right: Detail views based on the geometries as depicted in Fig. 4 showing the large volume on top and the small volume at the bottom.

composite cathode side, and the (dis-)charge boundary condition presented in Eq. (35) to the anode side. However, this approach is only possible if merely one composite electrode is part of the cell setup and thereby limits the flexibility of the application of the model. The second possibility would be to replace Eq. (35) by an a priori unknown time dependent potential, being adapted in a way, that the desired constant current is retained. A similar approach, where the time dependent potential was set on the complete particle surface, has already been applied in [36]. Yet, this approach leads to another constraint that has to be fulfilled and solved for during the non-linear solution process. An additional drawback of this approach can be that it is very complicated to obtain the linearization of this constraint with respect to the primary variables. Thus, convergence of this constraint inside the nonlinear solution procedure can be deteriorated. Besides the already stated individual drawbacks of those two alternative solution procedures, both additionally have the disadvantage that the mechanical influence of the current collectors is neglected, and that further effects like a contact resistance (see e.g. Eq. (30)) cannot be applied easily. Therefore, we suggest to explicitly model the current collectors in ASSB cell simulations.

4.2.3. Validation of the physical model

Below we conduct a brief comparison of the cell potential progression of our model to the one published in [18]. To allow for a fair comparison of the models, the computational domain as already discussed in Section 4.1.1 and visualized in Fig. 3, is tailored to match their setup as close as possible. This means that the dimensions, statistical distribution of the active material radii, and the volume shares within the composite cathode are selected equal. In the following we investigate two different scenarios. Since in [18] mechanical effects are not incorporated, we also do not consider the lithiation dependent volume changes in the first case called "no volume change" hereinafter. The second variation named "volume change" is taking the volume changes due to lithiation into account to also enable the quantification of the mechanical effect for the realistic geometry to gain additional insights compared to [18]. Moreover, the ASSB cell is discharged using a constant current at a C-rate of 0.1 until 2.8 V. For this investigation we changed the choice of the cutoff voltage from 2.6 V to 2.8 V as the reference solution of [18] is displayed until this value. In Fig. 9 the progression of the cell voltage curve from [18] and ours from the "no volume change" scenario shows a very good agreement during discharge. Both simulations result in approximately the same discharge capacity of 155 mAh/g with a relative deviation of only about 1%. The geometry used in these simulations is one sample of an underlying stochastic process that is constructed such that global geometric quantities of the cell, e.g. the particle size distribution of the NMC active material, match the ones as provided in [18]. Consequently, the computational domain differs from [18] as both are only realizations of an inherent random process. Nevertheless, considering this discrepancy the results are in very good agreement.

The comparison of the "no volume change" and "volume change" scenario reveals that the consideration of mechanical effects also has an influence on the electrochemical performance of the system. Namely, that the model including the volume expansion allows for larger discharge times and therefore a bigger discharge capacity. Here, the achieved discharge capacity increases by approximately 4%. This is already one argument that the incorporation of mechanical effects is important for a precise analysis of ASSB cells motivating the subsequent section for further investigations in this regard. Of course, there are more reasons for this incorporation as it also allows investigating local stress states and their influence on electrochemical transport properties, the investigation of the effect of different casings (see Section 4.3) or external pressure states, or detrimental scenarios like local contact losses to name just some.
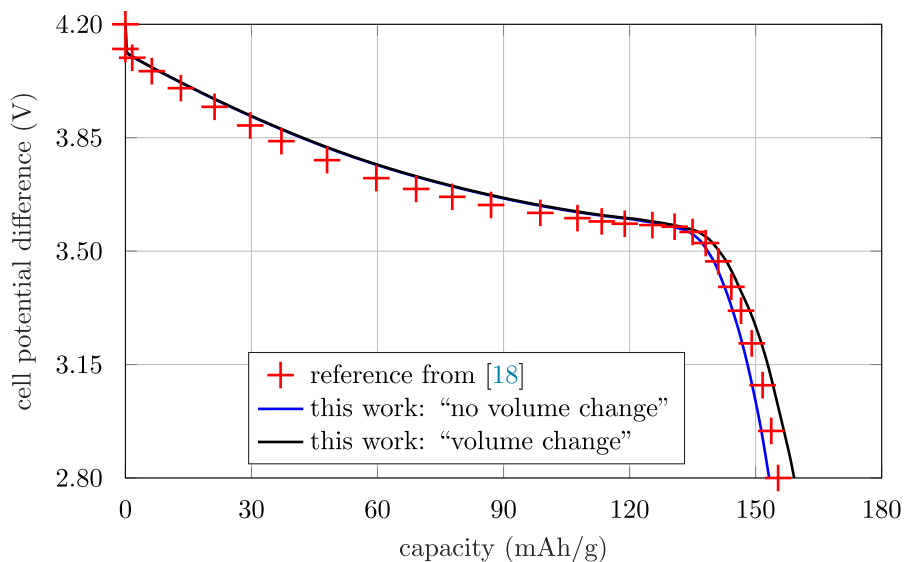

Fig. 9. Comparison of cell potential difference over discharge capacity for the realistic geometry.

4.3. Investigation of the influence of the mechanical setup on ASSB cells

In this section we first perform a detailed investigation of the influence of the mechanical setup on the electrochemical performance based on the simplified geometry. Then we investigate the influence of the mechanical setup on the mechanical state based on the realistic geometry.

4.3.1. Influence of the mechanical setup on the electrochemical performance based on a simplified ASSB cell geometry

In the following we investigate the influence of the mechanical setup on the performance of the battery cell including current collectors as shown in Fig. 4. The cell is again discharged at a constant current of 0.5 C until 2.6 V is reached. In order to examine the influence of the solid mechanics on the system performance we conduct two variations of the original problem setup. Subsequently, we refer to the original setup with the term "clamping". As a first variant we replace the infinitely stiff external support at the anode side current collector by an infinitely soft external support. This scenario is named "no clamping" in the ensuing paragraph and is modeled by replacing the Dirichlet boundary condition in normal direction by a homogeneous Neumann boundary condition. Those cases represent the extreme cases concerning mechanical boundary conditions, since in reality nothing is infinitely stiff or soft. For the second variation we disable the volume change due to lithiation what we hereinafter call "no volume change".

Fig. 10 shows the progression of the cell potential difference over discharge time for the three described scenarios. Due to the fact that the initialization is identical all curves feature a very similar progression in the beginning. However, over time the influence of the altered mechanical setups on the discharge behavior is increasing. The plot shows that the longest discharge times are achieved in the "clamping" case, whereas the "no volume change" setup features the shortest discharge time. The "no clamping" scenario, where the battery can freely decrease its thickness lies between the other cases. Since here we do not yet consider the potentially important influence of mechanical deformation or stresses on transport properties or interface kinetics explicitly, this difference has to originate from the change of the domains due to mechanical deformations. To verify this statement we plot the thicknesses of the battery cell components over time for the different mechanical setups. For the "no volume change" case (cf. graphs with ∘ symbols in Fig. 11) we do not see a change in the thickness of the battery components. This is the expected behavior since the lithiation dependent volume expansion is the origin of mechanical deformations, meaning that without volume expansion no deformations are anticipated. In the "no clamping" scenario (see graphs with + symbols in Fig. 11) the anode side current collector can move freely. Thus, no significant axial stresses arise in the battery cell leading to only negligible elastic deformations of all battery components. However, the thickness of the anode is significantly decreasing as lithium is stripped during discharging. Finally, in the last scenario we observe the effect of the assumptions that on the one hand the total volume of the battery cell remains constant due to the infinitely stiff support and on the other hand the different battery components cannot separate. This means that in a real setting the adhesive forces between the battery components would need to be strong enough that no spatial separation occurs. Consequently, the decrease in thickness of the anode due to stripping of lithium during discharging has to be compensated by an elastic deformation of all components leading to an increase in their thicknesses (see Fig. 11). From the fact that the thickness of the anode is always larger compared to the "no clamping" scenario, even though more lithium is stripped due to the longer discharge time, we can conclude that also the lithium metal anode is elastically deformed towards larger thicknesses.

However, the observed changes in thickness are counterintuitive to the larger charging times. A thicker solid electrolyte leads to more internal resistance of the cell and thus to more potential drop within the electrolyte. In theory this should result in shorter discharge times leading to the conclusion that there has to be another effect that overcompensates this. Fig. 12 shows that the mechanical setup indeed has an influence on the concentration distribution at about 10% SoC, i.e. close to the end of the discharge process. Especially the concentration at the surface is affected, which in turn influences the lithiation state dependent equilibrium
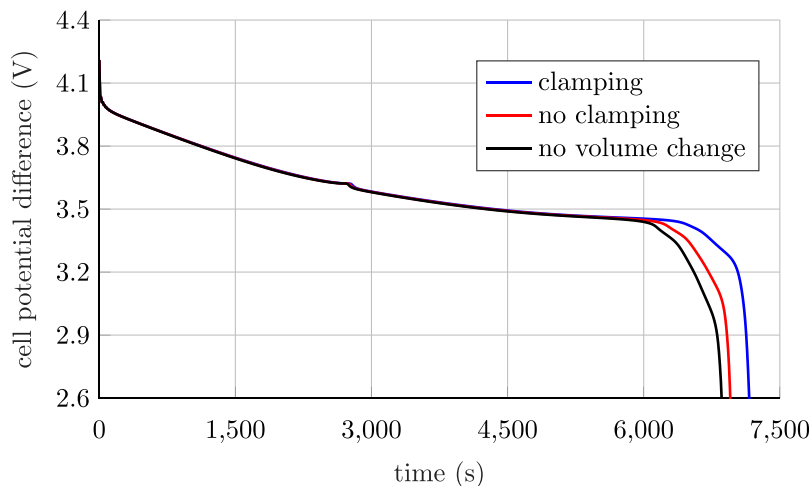

Fig. 10. Comparison of cell voltage progressions over discharge time for different mechanical setups.
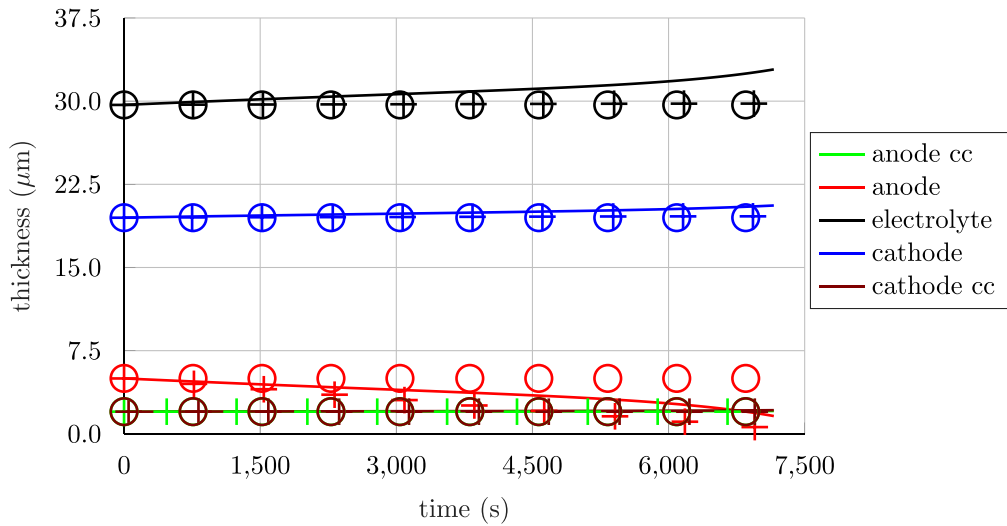
Fig. 11. Comparison of thicknesses of components for different mechanical setups over discharge time. The solid line depicts the "clamping" setting, whereas the symbols + and ◦ denote the scenarios "no clamping" and "no volume change", respectively.
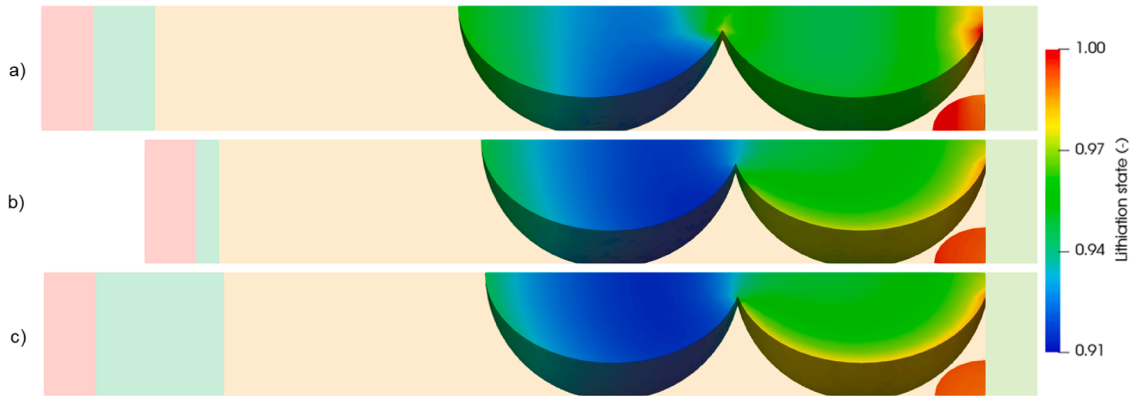

Fig. 12. Comparison of the influence of the mechanical setup on the lithiation state distribution at about 10% SoC during discharging. Subfigure (a) shows the "clamping" case, subfigure (b) the "no clamping" scenario, and subfigure (c) the "no volume change" variation.

potential (cf. Fig. B.1). As the equilibrium potential at the cathode side is a major contribution to the overall cell potential difference also the cell voltage is influenced. By analyzing Fig. 12 we see that this actually has to be the dominant effect. The simulation with the shortest discharge time, i.e. the "no volume change" scenario, shows the largest degree of lithiation at the interface (vid Fig. 12 c). In contrast, the simulation with the longest discharge time depicts the smallest lithiation state at the interface (cf. Fig. 12 a) and the third scenario lies in between those two cases.

To conclude, we again found that the mechanical setup has an effect on the discharge time, which varied by about 5% in this case. A similar result was already shown for the realistic geometry in Section 4.2.3. So the influence of the mechanical setup on the electrochemical performance of the ASSB cell is revealed for both investigated computational domains, highlighting the importance to consider mechanical effects to enable a precise analysis of ASSB cells even when potentially important features like stress dependent electrochemical transport properties, or local contact loss between two phases are not yet taken into account.

4.3.2. Influence of the mechanical setup on the mechanical state based on a realistic ASSB cell geometry

Now we investigate the influence of the mechanical boundary conditions on the mechanical response of the ASSB cell in more detail. Therefore, we employ the realistic geometry (see Fig. 3) and discharge the cell at a constant current of 0.1 C until 2.6 V is reached. Again, we compare the results of a simulation using an ideally stiff external mechanical support in axial direction of the battery named "clamping" to those with an ideally soft axial external boundary condition. Subsequently, the latter scenario is referred to using "no clamping". First we analyze the surface share of the cathode active material surface that experiences tensile stresses during the discharge process. Tensile stresses prevail if the normal projection of the Cauchy stress tensor is positive ($t = \boldsymbol{n} \cdot \boldsymbol{\sigma} \cdot \boldsymbol{n} > 0$). We think that this is a highly relevant mechanical quantity because all interfacial areas under tensile stresses are possible places for loss of

contact if e.g. adhesive forces are negligible or exceeded. Once a delamination of active material and solid electrolyte has taken place locally, those surfaces cannot participate in the charge transfer reaction anymore. Consequently, this largely effects the electro-chemical field by e.g. increasing the internal resistance of the battery. Due to the mechanical boundary conditions in the "no clamping" case we do not have significant tensile stresses emerging within the battery cell. Thus, the cathode side surface share experiencing tensile stresses constantly remains at a small value of approximately 2.5% during the discharge time. In the "clamping" scenario this is completely different due to the combination of the mechanical boundary and interface conditions as well as the operating condition of the battery cell. Since we are discharging the ASSB cell the thickness of the lithium metal anode significantly reduces. Furthermore, as the mechanical boundary and interface conditions enforce the volume of the ASSB cell to be constant, elastic tensile stresses need to arise to compensate for the decrease of thickness due to lithium metal stripping from the anode. Hence, the tensile stresses within the battery constantly increase during discharging, resulting in a non-linearly increasing surface share under tensile stress (cf. Fig. 13).

Remark. The presented results do not yet include the influence of local mechanical tensile stresses at the interfaces on the charge transfer. However, as already mentioned above local delamination inhibits local charge transfer reactions. This would result in elongated paths for charge and mass transfer and therefore in a potentially severe deterioration of the cell performance. Yet, such effects are beyond the scope of this work and will be addressed in upcoming research activities.

Please note that the results presented in Fig. 13 are only showing the surface share exhibiting tensile stresses at the cathode active material surface. It does not include the anode side, which in both cases would feature an (almost) complete delamination using these mechanical boundary conditions. Consequently, a simulation including the aforementioned influence of the mechanical tensile stresses at the interfacial charge transfer would nearly terminate immediately. Instead, it rather points out the well-known fact that such systems have to be operated under significant pre-stress to overcompensate at least the main part of the presented tensile interface stresses. Moreover, it indicates that the mechanical boundary conditions, e.g. the measuring device in an experiment, can have a significant influence on local mechanical quantities and thereby on the cell performance. Finally, it shows that the proposed model can be used to quantify the necessary mechanical pre-stress to prevent the occurrence of tensile stresses at the interface during cycling.

Lastly we show that the mechanical stress distribution is inhomogeneous and anisotropic within the cathode active material particles. To do so, we use the already described "clamping" case. As the simulation domain is too large to be able to depict this comprehensively, we use a small cut from the composite cathode particles to do the visualization. The position of the cut within the composite cathode is shown in Fig. 14 in green color. To ease orientation within the plot, the cathode side current collector and the cathode particles are shown transparent. Super-quadratic tensor glyphs are then used to depict the evolution of the mechanical stress state within the cathode particles. They base on a singular value decomposition of the stress tensor, i.e. its eigenvalues and eigenvectors. The glyphs are then created such that the orientation is based on the eigenvectors and their scaling on the corresponding eigenvalues. A spherical shape of the glyph represents an isotropic stress state, whereas a needle- or plate-like shape indicates significant anisotropy and its preferential direction. Fig. 15 shows a detail view of the small cluster of active material particles that are highlighted non-transparently in Fig. 14. Specifically for the middle particle, it can be seen that in different regions of the particle the preferential directions point in different directions. On the one hand, this indicates an anisotropic stress state as preferential directions are clearly visible. On the other hand, it also depicts an inhomogeneous mechanical state since the anisotropy is spatially varying. The preferential direction always points towards the surrounding cathode active material particles. This is reasonable as the cathode active material particles are the mechanically stiffest component within the composite cathode. Hence, they also transfer the main share of the mechanical load. Furthermore, it is observable that the magnitude of the mechanical stresses generally increase towards regions where particles are in contact. As those are the regions in which the geometry of the particles tapers off, the mechanical notch effect
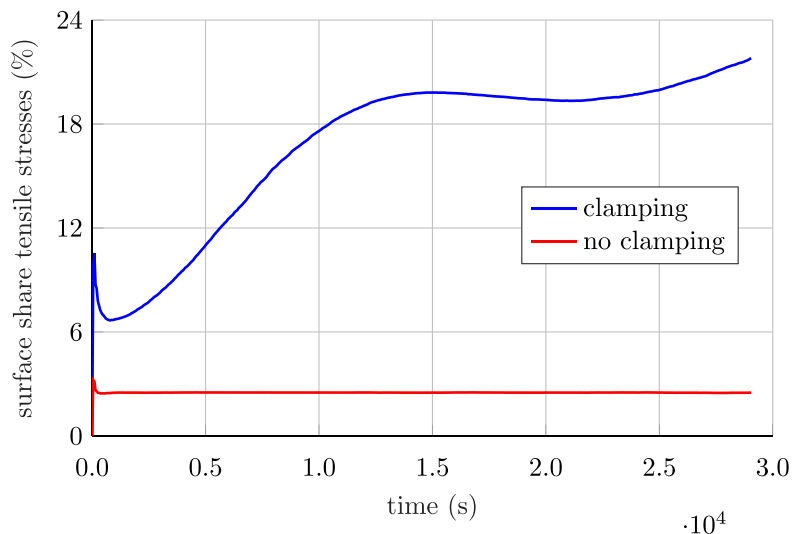

Fig. 13. Influence of mechanical boundary conditions on the cathode active material surface share that shows tensile stresses.
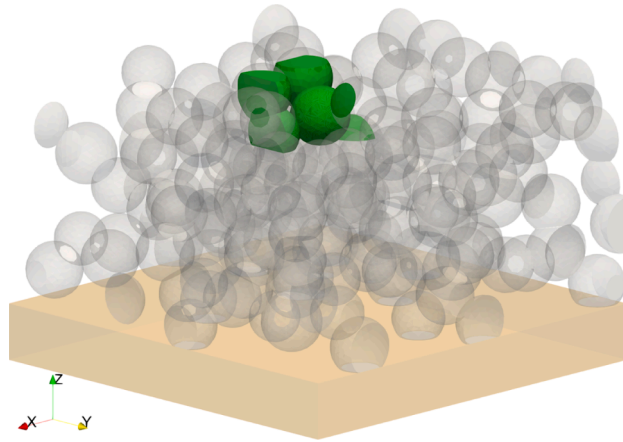
Fig. 14. Position of the cut volume within the composite cathode particles in green color used to visualize the mechanical stresses. (For interpretation of the references to color in this figure legend, the reader is referred to the web version of this article.)

leads to larger local mechanical stresses there as expected.

The proposed model thus also enables to investigate the three-dimensional stress state within an ASSB during operation. This information can be utilized in multiple ways, e.g. to evaluate whether mechanical failure mechanisms are likely to occur or to add further coupling effects like deformation dependent electrochemical transport properties as deduced from detailed atomistic simulations in [68].

5. Conclusion

Within this work a novel electro-chemo-mechanically coupled finite element formulation for microstructure resolved ASSB is introduced. The proposed model takes into account the solid mechanics by considering the conservation of linear and angular momentum and the electrochemical field by incorporating mass and charge conservation. It couples both fields by lithiation dependent volume changes of the active materials and the consideration of mechanical deformations in the equations describing conservation of mass and charge. The model is derived from non-linear continuum mechanics and thus capable to account for large deformations including a multiplicative split of the deformation gradient to consider large lithiation dependent volume changes as e.g. reported in [28,29]. To also enable large deformations for the conservation of mass we apply an ALE formulation. We then discuss the central steps to deduce the equations for the employed finite element method as well as the monolithic solution procedure to solve the resulting nonlinear system of equations. In the numerical examples we first show that our model is indeed capable to conserve mass and charge on deformed meshes before we point out that the explicit incorporation of current collectors in ASSB simulations is necessary to obtain reliable results. On top of that we showed that the results of our model match the results of [18] reasonably well if we also do not
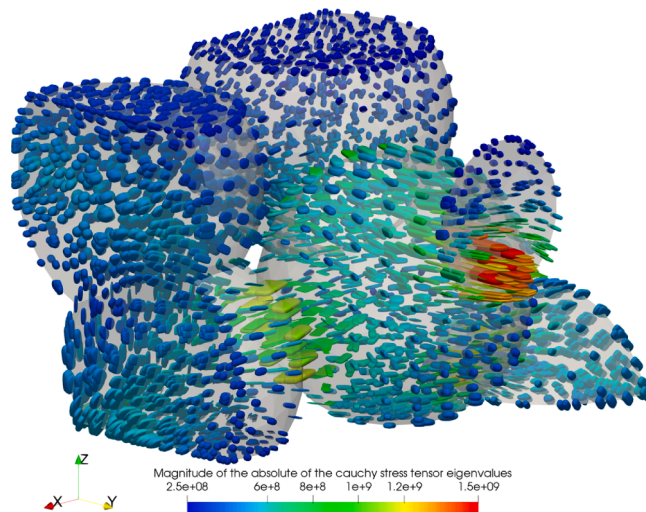

Fig. 15. Super-quadratic tensor glyphs applied to the absolute of the Cauchy stress tensor to visualize the mechanical stress state within the cut of the cathode particles at the end of the discharge process.

consider mechanical effects in our formulation. Moreover, it is presented that the incorporation of mechanical effects has an influence on the discharge behavior of an ASSB cell even though coupling effects like delamination of the active material and solid electrolyte are not yet considered in the model. However, such effects are not only reported in literature [4], but also indicated by our mechanical analysis of the simulation results. To sum up we could show that it is vital to incorporate electrochemical and mechanical effects as well as their coupling to ensure precise results of ASSB simulations.

For future research we propose to further increase the coupling of electrochemistry and solid mechanics by adding other relevant effects of electro-chemo-mechanics. The most obvious effect in this regard is the delamination of active materials and solid electrolyte. But also the dependence of the electrochemical transport kinetics on the mechanical deformation state as proposed by [68] will be an important step to enable the quantification of this effect deduced on an atomistic scale on the electrochemical performance on the cell level. Moreover, we believe that the incorporation of inhomogeneous lithium deposition and stripping at the lithium metal anode, and grain boundary transport mechanisms on resolved solid electrolyte grains are other effects of particular importance.

Funding

Declaration of competing interest

The authors declare that they have no known competing financial interests or personal relationships that could have appeared to influence the work reported in this paper.

Data availability

The result data of the simulations is made available via the Zenodo record 10.5281/zenodo.8386387.

Appendix A. Details on the derivation of the mass conservation equation in the solid electrolyte

From Eq. (19) to Eq. (21) the fourth term vanishes within the electrolyte domain. This is due to the application of the divergence to a product of a scalar field Θ and a vector field $\boldsymbol{v}$ reading:

$$\nabla \cdot (\Theta \boldsymbol{v}) = \Theta \nabla \cdot \boldsymbol{v} + \boldsymbol{v} \cdot \nabla \Theta \,. \tag{A.1}$$

Application of Eq. (A.1) to the fourth term of Eq. (19) leads to:

$$-\nabla \cdot \left(\frac{zFD}{RT} c \nabla \Phi \right) = -\frac{zFD}{RT} c \, \nabla \cdot \nabla \Phi - \frac{zFD}{RT} \nabla \Phi \cdot \nabla c \,. \tag{A.2}$$

The first term of the right-hand side is zero, due to the charge conservation Eq. (14), whereas the second term equals zero since no gradients in concentration emerge within the solid electrolyte. Consequently, this term vanishes, as described in Section 2.2.3.

Appendix B. Model parameters

In this section all values of the material, geometric, or initial parameters that are necessary to perform the simulations are presented. We start with listing the material parameters and initial conditions of the electrochemical field. Finally, the geometric dimensions of the different computational domains are given.

Table B.1
Parameters of the inelastic deformation used in the simulations.

parameter	value	unit
Cathode: NMC622		
a_0	0.000444577043098	–
a_1	−1.24116361022373	–
a_2	9.30461909734883	–
a_3	−29.44977325195	–
a_4	49.1126838772603	–
a_5	−45.1097641074935	–
a_6	21.5994362668471	–
a_7	−4.21656846170118	–
Anode: lithium		
g	$1.2998 \cdot 10^{-5}$	$\frac{\text{m}^3}{\text{mol}}$

B.1. Material parameters and initial conditions

The volume changes modeled using inelastic deformations as described in Eq. (22) and Eq. (23) have to be parameterized. Hereby, $f(\chi)$ is a polynomial fit of the following form:

$$f(\chi) = \sum_{n=0}^{7} a_i \chi^i \tag{B.3}$$

to the data from [5] as shown in Fig. 2. The parameter $g = \frac{M_{Li}}{\rho_{Li}}$ from Eq. (23) as well as the coefficients a_i are listed in the Table B.1.

Moreover, Table B.2 provides the necessary parameters to define the solid mechanics problem of the ASSB. As the density of NMC622 is not provided in [18] it is calculated to obtain a consistent parameter set as follows:

$$\rho = \frac{c_{max} M_{max}}{\chi_{max}}. \tag{B.4}$$

Table B.3 lists all required data needed for the electrochemistry problem. As usual, the SoC is defined based on the limiting electrode which is the cathode in this case. We assume that the SoC of the battery at the initial state is 100% resulting in $\chi_{100\%} = c^0/c_{max}$. Moreover, we define that the fully discharged state corresponds to the fully lithiated state $\chi_{0\%} = \chi_{max}$. For completeness, we repeat the lithiation dependent electronic conductivity of NMC622 from [18]:

$$\sigma(x) = 100 \, exp\big(-202.90 \, x^4 + 322.38 \, x^3 - 178.23 \, x^2 + 50.06 \, x - 13.47 \big), \tag{B.5}$$

with $x = 1 - \chi$, and the lithiation dependent diffusion coefficient of NMC622 from [18]:

$$\begin{aligned}
D(\chi) = \frac{1}{1000} exp \bigg(& 9.3764575854 \cdot 10^5 \cdot \chi^9 - 5.4262087319 \cdot 10^6 \cdot \chi^8 \\
& + 1.3688556703 \cdot 10^7 \cdot \chi^7 - 1.9734363260 \cdot 10^7 \cdot \chi^6 + 1.7897244160 \cdot 10^7 \cdot \chi^5 \\
& - 1.0576735297 \cdot 10^7 \cdot \chi^4 + 4.0688465295 \cdot 10^6 \cdot \chi^3 - 9.8167452940 \cdot 10^5 \cdot \chi^2 \\
& + 1.3468923578 \cdot 10^5 \cdot \chi - 8.0270847914 \cdot 10^3 \bigg).
\end{aligned} \tag{B.6}$$

Fig. B.1 shows the lithiation dependent open circuit potential Φ_0 of the cathode material NMC622 against lithium, based on [67]. It is given by:

$$\Phi_0(\chi) = 13.4905 - 10.96038\,\chi + 8.203617\,\chi^{1.358699} - 3.10758 \cdot 10^{-6} exp(127.1216\,\chi - 114.2593) - 7.033556\,\chi^{-0.03362749}. \tag{B.7}$$

Finally, the initial conditions of the electrochemical field are provided in Table B.4. The initial concentration of the lithium metal

Table B.2
Mechanical material parameters used for the simulations.

parameter	value	unit	description	source
Cathode side current collector: aluminum				
E	$7.00 \cdot 10^{10}$	Pa	Young's modulus	[69]
ν	0.35	–	Poisson's ratio	[69]
ρ	$2.70 \cdot 10^3$	$\frac{kg}{m^3}$	density	[70]
Cathode: NMC622				
E	$1.75 \cdot 10^{11}$	Pa	Young's modulus	[71]
ν	0.3	–	Poisson's ratio	[72–74]
ρ	$5.03 \cdot 10^3$	$\frac{kg}{m^3}$	density	Eq. (B.4)
Electrolyte: β-LPS				
E	$2.89 \cdot 10^{10}$	Pa	Young's modulus	[75]
ν	0.27	–	Poisson's ratio	[75]
ρ	$1.88 \cdot 10^3$	$\frac{kg}{m^3}$	density	[76]
Anode: lithium				
E	$4.90 \cdot 10^9$	Pa	Young's modulus	[77] based on [78]
ν	0.42	–	Poisson's ratio	[77] based on [78]
ρ	$5.34 \cdot 10^2$	$\frac{kg}{m^3}$	density	[79]
Anode side current collector: copper				
E	$1.30 \cdot 10^{11}$	Pa	Young's modulus	[69]
ν	0.34	–	Poisson's ratio	[69]
ρ	$8.96 \cdot 10^3$	$\frac{kg}{m^3}$	density	[79]

Table B.3
Electrochemical material parameters used for the simulations.

parameter	value	unit	description	source
Cathode side current collector: aluminum				
σ	$3.77 \cdot 10^7$	$\frac{S}{m}$	electronic conductivity	[70]
$R_{contact}$	$2.0 \cdot 10^{-3}$	$\Omega\,m^2$	contact resistance	assumed
Cathode: NMC622				
σ	Eq. (B.5)	$\frac{S}{m}$	electronic conductivity	[18]
D	Eq. (B.6)	$\frac{m^2}{s}$	diffusion coefficient	[18]
Φ_0	Fig. B.1	V	open circuit potential	[67]
i_0	4.98	$\frac{A}{m^2}$	exchange current density factor	adapted from [18]
α_a	0.5	–	anodic symmetry coefficient	[18]
c_{max}	$5.19 \cdot 10^4$	$\frac{mol}{m^3}$	maximum concentration	[18]
χ_{max}	1.0	–	maximum lithiation state	[18]
$\chi_{0\%}$	1.0	–	lithiation state at 0% SoC	assumed
$\chi_{100\%}$	$4.04 \cdot 10^{-1}$	–	lithiation state at 100% SoC	assumed
Electrolyte: β-LPS				
κ	$1.20 \cdot 10^{-2}$	$\frac{S}{m}$	ionic conductivity	[18]
t_{el}	1.0	–	lithium-ion transference number	[18]
Anode: lithium				
σ	$1.00 \cdot 10^5$	$\frac{S}{m}$	electronic conductivity	[18]
Φ_0	0.0	V	open circuit potential	[18]
i_0	8.87	$\frac{A}{m^2}$	exchange current density factor	[18]
α_a	0.5	–	anodic symmetry coefficient	[18]
Anode side current collector: copper				
σ	$5.81 \cdot 10^7$	$\frac{S}{m}$	electronic conductivity	[70]
$R_{contact}$	$2.0 \cdot 10^{-3}$	$\Omega\,m^2$	contact resistance	assumed
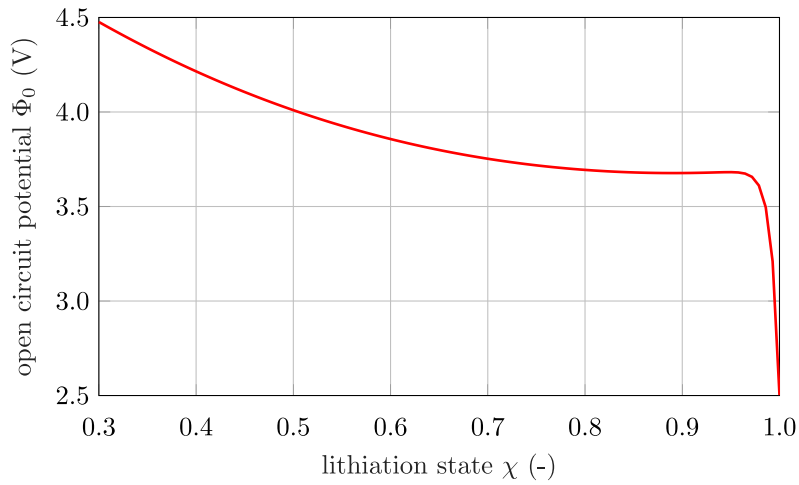
Fig. B.1. Open circuit potential of NMC622 as a function of the lithiation state based on [67].

anode is calculated based on the assumption of a pure substance from:

$$c = \frac{\rho}{M} \ . \tag{B.8}$$

B.2. Geometric parameters

Now we present the geometric properties of the different computational domains as presented in Section 4.1.1. Table B.5 shows the dimensions of both the simplified and the realistic geometries. Lastly, the properties of the composite cathode are given in Table B.6.

Table B.4
Electrochemical initial conditions used for the simulations.

domain	initial concentration c^0	unit	source
cathode	$2.10 \cdot 10^4$	$\frac{mol}{m^3}$	[18]
electrolyte	$1.03 \cdot 10^4$	$\frac{mol}{m^3}$	[18]
anode	$7.69 \cdot 10^4$	$\frac{mol}{m^3}$	Eq. (B.8)

Table B.5
Geometric dimensions used for the simulations.

quantity	unit	simplified geometry	realistic geometry
lateral dimensions	μm	–	75.0
thickness cathode side current collector	μm	2.0	10.0
thickness composite cathode	μm	19.5	40.0
thickness solid electrolyte separator	μm	10.0	425.0
thickness anode	μm	5.0	120.0
thickness anode side current collector	μm	2.0	10.0

According to [18] the active material secondary particles are spherical and exhibit a diameter of around 10 μm. For the realistic geometry, the diameter distribution is therefore approximated by a log-normal distribution:

$$f(\overline{d}|\mu,\sigma) = \frac{1}{\overline{d}\sigma\sqrt{2\pi}}exp\left(\frac{-(log\overline{d}-\mu)^2}{2\sigma^2}\right) \qquad \text{for}\overline{d} > 0\,, \tag{B.9}$$

with the mean μ and standard deviation σ of the normally distributed logarithm of the variable. As the log-normal distribution is unit-less, the unit of the diameter d is retained by $\overline{d} = d/1 \quad$ μm.

Appendix C. Linearization of the multiplicative split based material formulation

To ensure quadratic convergence of the non-linear solution algorithm we need the linearization of the second Piola–Kirchhoff stresses w.r.t. the right Cauchy–Green tensor:

$$\mathbb{C} = 2\frac{\partial \boldsymbol{S}}{\partial \boldsymbol{C}}\,. \tag{C.10}$$

The definition of the second Piola–Kirchhoff stresses (see Eq. (3)) is the starting point of the derivation of the linearization:

$$\boldsymbol{S} = 2\, det\boldsymbol{F}_{\text{in}}\boldsymbol{F}_{\text{in}}^{-1} \cdot \frac{\partial \varPsi_{\text{el}}}{\partial \boldsymbol{C}_{\text{el}}} \cdot \boldsymbol{F}_{\text{in}}^{-\text{T}}\,.$$

Rewriting the formulation by making use of factors γ_i as defined in [45] we get:

$$\boldsymbol{S} = det\boldsymbol{F}_{\text{in}}\left(\gamma_1 \boldsymbol{C}_{\text{in}}^{-1} + \gamma_2 \boldsymbol{C}_{\text{in}}^{-1} \cdot \boldsymbol{C} \cdot \boldsymbol{C}_{\text{in}}^{-1} + \gamma_3 \boldsymbol{C}^{-1}\right)\,. \tag{C.11}$$

By using the factors δ_i and the tensor product $\odot$ from [45] the linearization reads:

$$\begin{aligned}
\mathbb{C} = det\boldsymbol{F}_{\text{in}}\big[&\delta_1\left(\boldsymbol{C}_{\text{in}}^{-1} \otimes \boldsymbol{C}_{\text{in}}^{-1}\right) + \delta_2\left(\boldsymbol{C}_{\text{in}}^{-1} \otimes \boldsymbol{C}_{\text{in}}^{-1} \cdot \boldsymbol{C} \cdot \boldsymbol{C}_{\text{in}}^{-1} + \boldsymbol{C}_{\text{in}}^{-1} \cdot \boldsymbol{C} \cdot \boldsymbol{C}_{\text{in}}^{-1} \otimes \boldsymbol{C}_{\text{in}}^{-1}\right) \\
&+\delta_3\left(\boldsymbol{C}_{\text{in}}^{-1} \otimes \boldsymbol{C}^{-1} + \boldsymbol{C}^{-1} \otimes \boldsymbol{C}_{\text{in}}^{-1}\right) + \delta_4\left(\boldsymbol{C}_{\text{in}}^{-1} \cdot \boldsymbol{C} \cdot \boldsymbol{C}_{\text{in}}^{-1} \otimes \boldsymbol{C}_{\text{in}}^{-1} \cdot \boldsymbol{C} \cdot \boldsymbol{C}_{\text{in}}^{-1}\right) \\
+\delta_5\big(\boldsymbol{C}_{\text{in}}^{-1} \cdot \boldsymbol{C} &\cdot \boldsymbol{C}_{\text{in}}^{-1} \otimes \boldsymbol{C}^{-1} + \boldsymbol{C}^{-1} \otimes \boldsymbol{C}_{\text{in}}^{-1} \cdot \boldsymbol{C} \cdot \boldsymbol{C}_{\text{in}}^{-1}\big) + \delta_6\left(\boldsymbol{C}^{-1} \otimes \boldsymbol{C}^{-1}\right) + \delta_7\left(\boldsymbol{C}^{-1} \odot \boldsymbol{C}^{-1}\right) \\
&+\delta_8\left(\boldsymbol{C}_{\text{in}}^{-1} \odot \boldsymbol{C}_{\text{in}}^{-1}\right)\big]\,.
\end{aligned} \tag{C.12}$$

Table B.6
Geometric properties of the composite cathode.

quantity	unit	simplified geometry	realistic geometry
volumetric ratio active material to electrolyte	–	$42 : 58$	$47 : 53$
μ of log-normal distribution	–	–	2.3
σ of log-normal distribution	–	–	0.05
active material particle diameter	μm	10.0	–

Appendix D. Condensation procedure of the Lagrangian multipliers

We start by recalling the virtual energy contribution originating from the constraint enforcement as already stated in Eq. (48):

$$\delta W_{\text{constr}} = \sum_{j=1}^{n-1}\left[\quad \int_{\Gamma_c}\left(\delta\boldsymbol{\lambda}^{j\,\text{T}}\left(\boldsymbol{u}_{\text{def,m}} - \boldsymbol{u}_{\text{def,s}}^j\right) + \left(\delta\boldsymbol{u}_{\text{def,m}} - \delta\boldsymbol{u}_{\text{def,s}}^j\right)^{\text{T}}\boldsymbol{\lambda}^j\right)\text{d}\Gamma\right].\tag{D.13}$$

To obtain the discretized form, the continuous domain is subdivided into finite elements and the Lagrange multipliers and displacements are approximated as presented in Eq. (52):

$$\delta W_{\text{constr}} = \sum_{j=1}^{n-1}\left[\int_{\Gamma_c^h}\left(\delta\overline{\boldsymbol{\lambda}}^{j\,\text{T}}\boldsymbol{N}_\lambda^{\text{T}}\left(\boldsymbol{N}_u\overline{\boldsymbol{u}}_{\text{m}} - \boldsymbol{N}_u\overline{\boldsymbol{u}}_{\text{s}}^j\right) + \left(\boldsymbol{N}_u\delta\overline{\boldsymbol{u}}_{\text{m}} - \boldsymbol{N}_u\delta\overline{\boldsymbol{u}}_{\text{s}}^j\right)^{\text{T}}\boldsymbol{N}_\lambda\overline{\boldsymbol{\lambda}}^j\right)\text{d}\Gamma\right],\tag{D.14}$$

where the integral $\int_{\Gamma_c^h}$ symbolizes the sum of the element integrals. To simplify the notation we introduce the following terms:

$$\boldsymbol{R}_{\text{constr,m}}^j = \int_{\Gamma_c^h}\boldsymbol{N}_u^{\text{T}}\boldsymbol{N}_\lambda\overline{\boldsymbol{\lambda}}^j\text{d}\Gamma = \boldsymbol{M}_c^j\overline{\boldsymbol{\lambda}}^j, j = 1\dots n-1\,,\tag{D.15}$$

$$\boldsymbol{R}_\lambda^j = \int_{\Gamma_c^h}\boldsymbol{N}_\lambda^{\text{T}}\left(\boldsymbol{N}_u\overline{\boldsymbol{u}}_{\text{m}} - \boldsymbol{N}_u\overline{\boldsymbol{u}}_{\text{s}}^j\right)\text{d}\Gamma \quad = \boldsymbol{M}_c^{j\,\text{T}}\overline{\boldsymbol{u}}_{\text{m}} - \boldsymbol{M}_c^{j\,\text{T}}\overline{\boldsymbol{u}}_{\text{s}}^j \quad, j = 1\dots n-1\,,\tag{D.16}$$

$$\boldsymbol{R}_{\text{constr,s}}^j = \int_{\Gamma_c^h} -\boldsymbol{N}_u^{\text{T}}\boldsymbol{N}_\lambda\overline{\boldsymbol{\lambda}}^j\text{d}\Gamma = -\boldsymbol{M}_c^j\overline{\boldsymbol{\lambda}}^j, j = 1\dots n-1\,.\tag{D.17}$$

Further we introduce the standard solid mechanics residuals without mesh tying constraints separated into the different geometric regions, the interior of the body "i", the surface of the master body "m", and the surface of the slave body "s", each representing a subset of the already presented solid mechanics residual as follows $\boldsymbol{R}_{u_{\text{def}}}^{\text{T}} = \left[\boldsymbol{R}_{\text{std,i}}^{\text{T}}\,\boldsymbol{R}_{\text{std,m}}^{\text{T}}\,\boldsymbol{R}_{\text{std,s}}^{\text{T}}\right]$. On top of that, the residual of the electrochemistry problem "elch" is set up as $\boldsymbol{R}_{\text{elch}} = \left[\boldsymbol{R}_c^{\text{T}}\,\boldsymbol{R}_\phi^{\text{T}}\right]$. Summing all contributions and reordering all terms w.r.t. their virtual counterpart leads to the following expression of the virtual work:

$$\delta W = \delta\overline{\boldsymbol{\Psi}}_{\text{elch}}^{\text{T}}\boldsymbol{R}_{\text{elch}} + \delta\overline{\boldsymbol{u}}_{\text{i}}^{\text{T}}\boldsymbol{R}_{\text{std,i}} + \sum_{j=1}^{n-1}\left[\delta\overline{\boldsymbol{u}}_{\text{m}}^{\text{T}}\left(\boldsymbol{R}_{\text{std,m}} + \boldsymbol{R}_{\text{constr,m}}^j\right) + \delta\overline{\boldsymbol{u}}_{\text{s}}^{j\,\text{T}}\left(\boldsymbol{R}_{\text{std,s}}^j + \boldsymbol{R}_{\text{constr,s}}^j\right) + \delta\overline{\boldsymbol{\lambda}}^{j\,\text{T}}\boldsymbol{R}_\lambda^j\right] = 0\,.\tag{D.18}$$

Requesting arbitrary virtual perturbations results in the following nonlinear system of equations:

$$\begin{bmatrix} \boldsymbol{R}_{\text{std,i}} \\ \boldsymbol{R}_{\text{std,m}} + \sum_{j=1}^{n-1}\boldsymbol{R}_{\text{constr,m}}^j \\ \boldsymbol{R}_{\text{std,s}}^1 + \boldsymbol{R}_{\text{constr,s}}^1 \\ \vdots \\ \boldsymbol{R}_{\text{std,s}}^{n-1} + \boldsymbol{R}_{\text{constr,s}}^{n-1} \\ \boldsymbol{R}_{\text{elch}} \\ \boldsymbol{R}_\lambda^1 \\ \vdots \\ \boldsymbol{R}_\lambda^{n-1} \end{bmatrix} = \begin{bmatrix} \boldsymbol{0} \\ \boldsymbol{0} \\ \boldsymbol{0} \\ \vdots \\ \boldsymbol{0} \\ \boldsymbol{0} \\ \boldsymbol{0} \\ \vdots \\ \boldsymbol{0} \end{bmatrix}.\tag{D.19}$$

The additional contributions to the residuals affect the corresponding linearized system. To allow a concise presentation of the linearized system of equations we introduce the following abbreviations:

$$\frac{\partial\boldsymbol{R}_{\text{constr,m}}^j}{\partial\overline{\boldsymbol{\lambda}}^j} = \boldsymbol{M}_c^j\,,\quad \frac{\partial\boldsymbol{R}_{\text{constr,s}}^j}{\partial\overline{\boldsymbol{\lambda}}^j} = -\boldsymbol{M}_c^j\,,\quad \frac{\boldsymbol{R}_\lambda^j}{\partial\overline{\boldsymbol{u}}_{\text{m}}} = \boldsymbol{M}_c^j\,,\quad \frac{\boldsymbol{R}_\lambda^j}{\partial\overline{\boldsymbol{u}}_{\text{s}}^j} = -\boldsymbol{M}_c^j\,,\quad \frac{\partial\boldsymbol{R}_i}{\partial\boldsymbol{u}_i} = \boldsymbol{K}_{ii}\,, \frac{\partial\boldsymbol{R}_{\text{elch}}}{\partial\boldsymbol{u}_i} = \boldsymbol{K}_{\Psi i}\,,\quad \frac{\partial\boldsymbol{R}_i}{\partial\boldsymbol{\Psi}} = \boldsymbol{K}_{i\Psi}\,,$$

which are introduced into the stiffness matrix:

$$
\begin{bmatrix}
\boldsymbol{K}_{\mathrm{ii}} & \boldsymbol{K}_{\mathrm{im}} & \boldsymbol{K}_{\mathrm{is}}^{1} & \dots & \boldsymbol{K}_{\mathrm{is}}^{n-1} & \boldsymbol{K}_{\mathrm{i}\varPsi} & \boldsymbol{0} & \dots & \boldsymbol{0} \\
\boldsymbol{K}_{\mathrm{mi}} & \boldsymbol{K}_{\mathrm{mm}} & \boldsymbol{0} & \dots & \boldsymbol{0} & \boldsymbol{K}_{\mathrm{m}\varPsi} & \boldsymbol{M}_{\mathrm{c}}^{1} & \dots & \boldsymbol{M}_{\mathrm{c}}^{n-1} \\
\boldsymbol{K}_{\mathrm{si}}^{1} & \boldsymbol{0} & \boldsymbol{K}_{\mathrm{ss}}^{11} & \dots & \boldsymbol{0} & \boldsymbol{K}_{\mathrm{s}\varPsi}^{1} & -\boldsymbol{M}_{\mathrm{c}}^{1} & \dots & \boldsymbol{0} \\
\vdots & \vdots & \vdots & \ddots & \vdots & \vdots & \vdots & \ddots & \vdots \\
\boldsymbol{K}_{\mathrm{si}}^{n} & \boldsymbol{0} & \boldsymbol{0} & \dots & \boldsymbol{K}_{\mathrm{ss}}^{n-1} & \boldsymbol{K}_{\mathrm{s}\varPsi}^{n-1} & \boldsymbol{0} & \dots & -\boldsymbol{M}_{\mathrm{c}}^{n-1} \\
\boldsymbol{K}_{\varPsi\mathrm{i}} & \boldsymbol{K}_{\varPsi\mathrm{m}} & \boldsymbol{K}_{\varPsi\mathrm{s}}^{1} & \dots & \boldsymbol{K}_{\varPsi\mathrm{s}}^{n-1} & \boldsymbol{K}_{\varPsi\varPsi} & \boldsymbol{0} & \dots & \boldsymbol{0} \\
\boldsymbol{0} & \boldsymbol{M}_{\mathrm{c}}^{1} & -\boldsymbol{M}_{\mathrm{c}}^{1} & \dots & \boldsymbol{0} & \boldsymbol{0} & \boldsymbol{0} & \dots & \boldsymbol{0} \\
\vdots & \vdots & \vdots & \ddots & \vdots & \boldsymbol{0} & \boldsymbol{0} & \dots & \boldsymbol{0} \\
\boldsymbol{0} & \boldsymbol{M}_{\mathrm{c}}^{n-1} & \boldsymbol{0} & \dots & -\boldsymbol{M}_{\mathrm{c}}^{n-1} & \boldsymbol{0} & \boldsymbol{0} & \dots & \boldsymbol{0}
\end{bmatrix}_{j}
\begin{bmatrix}
\Delta\boldsymbol{u}_{\mathrm{i}} \\
\Delta\boldsymbol{u}_{\mathrm{m}} \\
\Delta\boldsymbol{u}_{\mathrm{s}}^{1} \\
\vdots \\
\Delta\boldsymbol{u}_{\mathrm{s}}^{n-1} \\
\Delta\boldsymbol{\varPsi} \\
\Delta\lambda^{1} \\
\vdots \\
\Delta\lambda^{n-1}
\end{bmatrix}_{j+1}
= -
\begin{bmatrix}
\boldsymbol{R}_{\mathrm{std,i}} \\
\boldsymbol{R}_{\mathrm{std,m}} + \sum_{j=1}^{n-1}\boldsymbol{R}_{\mathrm{constr,m}}^{j} \\
\boldsymbol{R}_{\mathrm{std,s}}^{1} + \boldsymbol{R}_{\mathrm{constr,s}}^{1} \\
\vdots \\
\boldsymbol{R}_{\mathrm{std,s}}^{n-1} + \boldsymbol{R}_{\mathrm{constr,s}}^{n-1} \\
\boldsymbol{R}_{\mathrm{elch}} \\
\boldsymbol{0} \\
\vdots \\
\boldsymbol{0}
\end{bmatrix}_{j}.
\tag{D.20}
$$

The next step is to condense out the displacements at the slave side of the interface. Therefore, we solve for the $j-$ th slave side displacement increment:

$$
\Delta\boldsymbol{u}_{\mathrm{s}}^{j} = -\boldsymbol{K}_{\mathrm{ss}}^{j\,-1}\left(\boldsymbol{K}_{\mathrm{si}}^{j}\Delta\boldsymbol{u}_{\mathrm{i}} + \boldsymbol{K}_{\mathrm{s}\varPsi}^{j}\Delta\boldsymbol{\varPsi} - \boldsymbol{M}_{\mathrm{c}}^{j}\Delta\lambda^{j} + \boldsymbol{R}_{\mathrm{std,s}}^{j} + \boldsymbol{R}_{\mathrm{constr,s}}^{j}\right), \quad j = 1..n-1\,.
\tag{D.21}
$$

By introducing these $n-1$ equations into the system (see Eq. (D.20)) the slave side displacements vanish. Applying the same strategy to the Lagrange multipliers leads to the final system of linear equations:

$$
\begin{bmatrix}
\boldsymbol{K}_{\mathrm{ii}} & \boldsymbol{K}_{\mathrm{im}} + \sum_{j=1}^{n-1}\boldsymbol{K}_{\mathrm{is}}^{j} & \boldsymbol{K}_{\mathrm{i}\varPsi} \\
\boldsymbol{K}_{\mathrm{mi}} + \sum_{j=1}^{n-1}\boldsymbol{K}_{\mathrm{si}}^{j} & \boldsymbol{K}_{\mathrm{mm}} + \sum_{j=1}^{n-1}\boldsymbol{K}_{\mathrm{ss}}^{j} & \boldsymbol{K}_{\mathrm{m}\varPsi} + \sum_{j=1}^{n-1}\boldsymbol{K}_{\mathrm{s}\varPsi}^{j} \\
\boldsymbol{K}_{\varPsi\mathrm{i}} & \boldsymbol{K}_{\varPsi\mathrm{m}} + \sum_{j=1}^{n-1}\boldsymbol{K}_{\varPsi\mathrm{s}}^{j} & \boldsymbol{K}_{\varPsi\varPsi}
\end{bmatrix}_{j}
\begin{bmatrix}
\Delta\boldsymbol{u}_{\mathrm{i}} \\
\Delta\boldsymbol{u}_{\mathrm{m}} \\
\Delta\boldsymbol{\varPsi}
\end{bmatrix}_{j+1}
=
\begin{bmatrix}
-\boldsymbol{R}_{\mathrm{std,i}} \\
-\boldsymbol{R}_{\mathrm{std,m}} - \sum_{j=1}^{n-1}\boldsymbol{R}_{\mathrm{std,s}}^{j} \\
-\boldsymbol{R}_{\mathrm{elch}}
\end{bmatrix}_{j}.
\tag{D.22}
$$

References

[1] P. Adelhelm, J. Janek, Zukunftstechnologien, in: R. Korthauer (Ed.), Handbuch Lithium-Ionen-Batterien, Springer Berlin Heidelberg, 2013, pp. 199–217 (Chapter 16).

[2] K.G. Gallagher, S.E. Trask, C. Bauer, T. Woehrle, S.F. Lux, M. Tschech, P. Lamp, B.J. Polzin, S. Ha, B. Long, Q. Wu, W. Lu, D.W. Dees, A.N. Jansen, Optimizing areal capacities through understanding the limitations of lithium-ion electrodes, J. Electrochem. Soc. 163 (2) (2015) A138–A149.

[3] S.P. Culver, R. Koerver, T. Krauskopf, W.G. Zeier, Designing ionic conductors: The interplay between structural phenomena and interfaces in thiophosphate-based solid-state batteries, Chem. Mater. 30 (13) (2018) 4179–4192.

[4] R. Koerver, I. Aygün, T. Leichtweiß, C. Dietrich, W. Zhang, J.O. Binder, P. Hartmann, W.G. Zeier, J. Janek, Capacity fade in solid-state batteries: Interphase formation and chemomechanical processes in nickel-rich layered oxide cathodes and lithium thiophosphate solid electrolytes, Chem. Mater. 29 (13) (2017) 5574–5582.

[5] R. Koerver, W. Zhang, L. de Biasi, S. Schweidler, A.O. Kondrakov, S. Kolling, T. Brezesinski, P. Hartmann, W.G. Zeier, J. Janek, Chemo-mechanical expansion of lithium electrode materials – on the route to mechanically optimized all-solid-state batteries, Energy Environ. Sci. 11 (8) (2018) 2142–2158.

[6] J. Janek, W.G. Zeier, A solid future for battery development, Nature Energy 1 (9) (2016).

[7] J.H. Teo, F. Strauss, F. Walther, Y. Ma, S. Payandeh, T. Scherer, M. Bianchini, J. Janek, T. Brezesinski, The interplay between (electro)chemical and (chemo) mechanical effects in the cycling performance of thiophosphate-based solid-state batteries, Mater. Futures 1 (1) (2022), 015102.

[8] B. Koohbor, L. Sang, Ö.Ö. Çapraz, A.A. Gewirth, N.R. Sottos, In situ strain measurement in solid-state Li-ion battery electrodes, J. Electrochem. Soc. 168 (1) (2021), 010516.

[9] C. Li, S. Yang, L. Xin, Z. Wang, Q. Xu, L. Li, S. Wang, In-situ characterization for solid electrolyte deformations in a lithium metal solid-state battery, J. Electrochem. Soc. 168 (7) (2021), 070551.

[10] G. Conforto, R. Ruess, D. Schröder, E. Trevisanello, R. Fantin, F.H. Richter, J. Janek, Editors' choice—quantification of the impact of chemo-mechanical degradation on the performance and cycling stability of NCM-based cathodes in solid-state Li-ion batteries, J. Electrochem. Soc. 168 (7) (2021), 070546.

[11] S. Ohno, R. Koerver, G. Dewald, C. Rosenbach, P. Titscher, D. Steckermeier, A. Kwade, J. Janek, W.G. Zeier, Observation of chemomechanical failure and the influence of cutoff potentials in all-solid-state Li–S batteries, Chem. Mater. 31 (8) (2019) 2930–2940.

[12] N. Riphaus, B. Stiaszny, H. Beyer, S. Indris, H.A. Gasteiger, S.J. Sedlmaier, Editors' choice—understanding chemical stability issues between different solid electrolytes in all-solid-state batteries, J. Electrochem. Soc. 166 (6) (2019) A975–A983.

[13] R. Bradbury, G.F. Dewald, M.A. Kraft, T. Arlt, N. Kardjilov, J. Janek, I. Manke, W.G. Zeier, S. Ohno, Visualizing reaction fronts and transport limitations in solid-state Li-S batteries via operando neutron imaging, ChemRxiv (2021).

[14] J. Tippens, J.C. Miers, A. Afshar, J.A. Lewis, F.J.Q. Cortes, H. Qiao, T.S. Marchese, C.V.D. Leo, C. Saldana, M.T. McDowell, Visualizing chemomechanical degradation of a solid-state battery electrolyte, ACS Energy Lett. 4 (6) (2019) 1475–1483.

[15] Z. Huang, S. Choudhury, N. Paul, J.H. Thienenkamp, P. Lennartz, H. Gong, P. Müller-Buschbaum, G. Brunklaus, R. Gilles, Z. Bao, Effects of polymer coating mechanics at solid-electrolyte interphase for stabilizing lithium metal anodes, Adv. Energy Mater. 12 (5) (2021), 2103187.

[16] D. Miranda, C. Costa, S. Lanceros-Mendez, Lithium ion rechargeable batteries: State of the art and future needs of microscopic theoretical models and simulations, J. Electroanal. Soc. 739 (2015) 97–110.

[17] A. Neumann, T.R. Hamann, T. Danner, S. Hein, K. Becker-Steinberger, E. Wachsman, A. Latz, Effect of the 3D structure and grain boundaries on lithium transport in garnet solid electrolytes, ACS Appl. Energy Mater. 4 (5) (2021) 4786–4804.

[18] A. Neumann, S. Randau, K. Becker-Steinberger, T. Danner, S. Hein, Z. Ning, J. Marrow, F.H. Richter, J. Janek, A. Latz, Analysis of interfacial effects in all-solid-state batteries with thiophosphate solid electrolytes, ACS Appl. Mater. Interfaces (2020).

[19] A.F. Bower, E. Chason, P.R. Guduru, B.W. Sheldon, A continuum model of deformation, transport and irreversible changes in atomic structure in amorphous lithium–silicon electrodes, Acta Mater. 98 (2015) 229–241. URL https://www.sciencedirect.com/science/article/pii/S1359645415005078.

[20] A.M. Boyce, E. Martínez-Pañeda, A. Wade, Y.S. Zhang, J.J. Bailey, T.M. Heenan, D.J. Brett, P.R. Shearing, Cracking predictions of lithium-ion battery electrodes by X-ray computed tomography and modelling, J. Power Sources 526 (2022), 231119. URL https://www.sciencedirect.com/science/article/pii/S0378775322001422.

[21] D. Carlstedt, K. Runesson, F. Larsson, L.E. Asp, On the coupled thermo–electro–chemo–mechanical performance of structural batteries with emphasis on thermal effects, Eur. J. Mech. A Solids 94 (2022), 104586.

[22] T. Hofmann, D. Westhoff, J. Feinauer, H. Andrä, J. Zausch, V. Schmidt, R. Müller, Electro-chemo-mechanical simulation for lithium ion batteries across the scales, Int. J. Solids Struct. 184 (2020) 24–39.

[23] M. Magri, B. Boz, L. Cabras, A. Salvadori, Quantitative investigation of the influence of electrode morphology in the electro-chemo-mechanical response of Li-ion batteries, Electrochim. Acta 405 (2022), 139778.

[24] T.H. Wan, F. Ciucci, Electro-chemo-mechanical modeling of solid-state batteries, Electrochim. Acta 331 (2020), 135355.

[25] B. Wu, W. Lu, A consistently coupled multiscale mechanical–electrochemical battery model with particle interaction and its validation, J. Mech. Phys. Solids 125 (2019) 89–111.

[26] Y. Zhao, R. Wang, E. Martínez-Pañeda, A phase field electro-chemo-mechanical formulation for predicting void evolution at the Li–electrolyte interface in all-solid-state batteries, J. Mech. Phys. Solids 167 (2022), 104999.

[27] T. Zhang, M. Kamlah, Mechanically coupled phase-field modeling of microstructure evolution in sodium ion batteries particles of Na_xFePO_4, J. Electrochem. Soc. 167 (2) (2020), 020508.

[28] L.Y. Beaulieu, K.W. Eberman, R.L. Turner, L.J. Krause, J.R. Dahn, Colossal reversible volume changes in lithium alloys, Electrochem. Solid-State Lett. 4 (9) (2001) A137.

[29] A. Timmons, J.R. Dahn, Isotropic volume expansion of particles of amorphous metallic alloys in composite negative electrodes for Li-ion batteries, J. Electrochem. Soc. 154 (5) (2007) A444–A448.

[30] Y. Bai, D.A. Santos, S. Rezaei, P. Stein, S. Banerjee, B.-X. Xu, A chemo-mechanical damage model at large deformation: numerical and experimental studies on polycrystalline energy materials, Int. J. Solids Struct. 228 (2021), 111099.

[31] G. Bucci, Y.-M. Chiang, W.C. Carter, Formulation of the coupled electrochemical–mechanical boundary-value problem, with applications to transport of multiple charged species, Acta Mater. 104 (2016) 33–51.

[32] M. Ganser, F.E. Hildebrand, M. Kamlah, R.M. McMeeking, A finite strain electro-chemo-mechanical theory for ion transport with application to binary solid electrolytes, J. Mech. Phys. Solids 125 (2019) 681–713.

[33] Y. Liu, K. Guo, C. Wang, J. Han, H. Gao, Concentration dependent properties and plastic deformation facilitate instability of the solid-electrolyte interphase in Li-ion batteries, Int. J. Solids Struct. 198 (2020) 99–109.

[34] X. Zhang, A. Krischok, C. Linder, A variational framework to model diffusion induced large plastic deformation and phase field fracture during initial two-phase lithiation of silicon electrodes, Comput. Methods Appl. Mech. Engrg. 312 (2016) 51–77.

[35] F. Hao, W. Wang, P.P. Mukherjee, Mechano-electrochemical interaction in solid-state lithium batteries, J. Electrochem. Soc. 167 (8) (2020), 080513.

[36] D. Bistri, C.V. Di Leo, Modeling of chemo-mechanical multi-particle interactions in composite electrodes for liquid and solid-state Li-ion batteries, J. Electrochem. Soc. 168 (3) (2021), 030515.

[37] Y. Huang, F. Zhang, Q.-A. Huang, Y. He, J. Zhang, Numerical investigation on diffusion-induced cracking in solid electrolyte of composite electrode and its impact on the Li-ion conductivity, J. Electrochem. Soc. 168 (12) (2021) 120506.

[38] X. Cai, Z. Guo, Influence of li concentration-dependent diffusion coefficient and modulus hardening on diffusion-induced stresses in anisotropic anode particles, J. Electrochem. Soc. 168 (1) (2021) 010517.

[39] G.F. Castelli, L. von Kolzenberg, B. Horstmann, A. Latz, W. Dörfler, Efficient simulation of chemical–mechanical coupling in battery active particles, Energy Technol. 9 (6) (2021), 2000835.

[40] L. Kolzenberg, A. Latz, B. Horstmann, Chemo-mechanical model of SEI growth on silicon electrode particles, Batteries & Supercaps 5 (2) (2021).

[41] W. Mai, A. Colclasure, K. Smith, A reformulation of the Pseudo2D battery model coupling large electrochemical-mechanical deformations at particle and electrode levels, J. Electrochem. Soc. 166 (8) (2019) A1330–A1339.

[42] D.J. Pereira, A.M. Aleman, J.W. Weidner, T.R. Garrick, A mechano-electrochemical battery model that accounts for preferential lithiation inside blended silicon graphite (Si/C) anodes, J. Electrochem. Soc. 169 (2) (2022), 020577.

[43] X. Zhang, M. Klinsmann, S. Chumakov, X. Li, S.U. Kim, M. Metzger, M.M. Besli, R. Klein, C. Linder, J. Christensen, A modified electrochemical model to account for mechanical effects due to lithium intercalation and external pressure, J. Electrochem. Soc. 168 (2) (2021), 020533.

[44] R. Fang, M. Kronbichler, M. Wurzer, W.A. Wall, Parallel, physics-oriented, monolithic solvers for three-dimensional, coupled finite element models of lithium-ion cells, Comput. Methods Appl. Mech. Engrg. 350 (2019) 803–835.

[45] G.A. Holzapfel, Nonlinear Solid Mechanics, Wiley John + Sons, 2000.

[46] L. de Biasi, A.O. Kondrakov, H. Geßwein, T. Brezesinski, P. Hartmann, J. Janek, Between scylla and charybdis: Balancing among structural stability and energy density of layered NCM cathode materials for advanced lithium-ion batteries, J. Phys. Chem. C 121 (47) (2017) 26163–26171.

[47] A.O. Kondrakov, A. Schmidt, J. Xu, H.G. wein, R. Mönig, P. Hartmann, H. Sommer, T. Brezesinski, J. Janek, Anisotropic lattice strain and mechanical degradation of high- and low-nickel NCM cathode materials for Li-ion batteries, J. Phys. Chem. C 121 (6) (2017) 3286–3294.

[48] M. Scheidler, T.W. Write, A continuum framework for finite viscoplasticity, Int. J. Plast. 17 (8) (2001) 1033–1085.

[49] E.A. de Souza Neto, D. Peric, D.R.J. Owen, Computational Methods for Plasticity: Theory and Applications, Wiley, 2008.

[50] S. Braun, C. Yada, A. Latz, Thermodynamically consistent model for space-charge-layer formation in a solid electrolyte, J. Phys. Chem. C 119 (39) (2015) 22281–22288.

[51] N.J.J. de Klerk, M. Wagemaker, Space-charge layers in all-solid-state batteries; important or negligible? ACS Appl. Energy Mater. 1 (10) (2018) 5609–5618.

[52] Y. Kato, S. Shiotani, K. Morita, K. Suzuki, M. Hirayama, R. Kanno, All-solid-state batteries with thick electrode configurations, J. Phys. Chem. Lett. 9 (3) (2018) 607–613.

[53] I.A. Sokolov, A.A. Il'in, Y.P. Tarlakov, N.A. Valova, A.A. Pronkin, Structure and physicochemical properties of glasses in the $Li_2S–LiPO_3$ system, Glass Phys. Chem. 29 (3) (2003) 282–290.

[54] I.A. Sokolov, N.A. Valova, Y.P. Tarlakov, A.A. Pronkin, Electrical properties and the structure of glasses in the $Li_2SO_4–LiPO_3$ system, Glass Phys. Chem. 29 (6) (2003) 548–554.

[55] S. Li, Z. Jiang, J. Han, Z. Xu, C. Wang, H. Huang, C. Yu, S.-J. Lee, P. Pianetta, H. Ohldag, J. Qiu, J.-S. Lee, F. Lin, K. Zhao, Y. Liu, Mutual modulation between surface chemistry and bulk microstructure within secondary particles of nickel-rich layered oxides, Nature Commun. 11 (1) (2020).

[56] L. Porz, T. Swamy, B.W. Sheldon, T. Rettenwander, T. Frömling, H.L. Thaman, S. Berendts, R. Uecker, W.C. Carter, Y.-M. Chiang, Mechanism of lithium metal penetration through inorganic solid electrolytes, Adv. Energy Mater. 7 (20) (2017), 1701003.

[57] A. Latz, J. Zausch, Thermodynamic derivation of a Butler–Volmer model for intercalation in Li-ion batteries, Electrochim. Acta 110 (2013) 358–362.

[58] A.M. Colclasure, R.J. Kee, Thermodynamically consistent modeling of elementary electrochemistry in lithium-ion batteries, Electrochim. Acta 55 (28) (2010) 8960–8973.

[59] R. Fang, P. Farah, A. Popp, W.A. Wall, A monolithic, mortar-based interface coupling and solution scheme for finite element simulations of lithium-ion cells, Internat. J. Numer. Methods Engrg. 114 (13) (2018) 1411–1437.

[60] M.W. Gee, U. Küttler, W.A. Wall, Truly monolithic algebraic multigrid for fluid–structure interaction, Internat. J. Numer. Methods Engrg. 85 (8) (2011) 987–1016.

[61] C. Danowski, V. Gravemeier, L. Yoshihara, W.A. Wall, A monolithic computational approach to thermo-structure interaction, Internat. J. Numer. Methods Engrg. 95 (13) (2013) 1053–1078.

[62] F. Verdugo, W.A. Wall, Unified computational framework for the efficient solution of n-field coupled problems with monolithic schemes, Comput. Methods Appl. Mech. Engrg. 310 (2016) 335–366.

[63] F. BACI, A comprehensive multi-physics simulation framework, 2022. URL https://baci.pages.gitlab.lrz.de/website/. (Accessed 14 December 2022).

[64] U. Ayachit, The ParaView Guide: A Parallel Visualization Application, Kitware, Inc., USA, 2015.

[65] U. The MathWorks, Inc., MATLAB R2020b (9.9.0.1495850), 2020.

[66] Coreform Cubit (Version 2021.3) [Computer software] Orem, UT: Coreform LLC. Retrieved from http://coreform.com.

[67] L.S. Kremer, A. Hoffmann, T. Danner, S. Hein, B. Prifling, D. Westhoff, C. Dreer, A. Latz, V. Schmidt, M. Wohlfahrt-Mehrens, Manufacturing process for improved ultra-thick cathodes in high-energy lithium-ion batteries, Energy Technol. 8 (2) (2019), 1900167.

[68] A. Moradabadi, P. Kaghazchi, J. Rohrer, K. Albe, Influence of elastic strain on the thermodynamics and kinetics of lithium vacancy in bulk LiCoO$_2$, Phys. Rev. Mater. 2 (1) (2018).

[69] L.B. Freund, S. Suresh, Thin Film Materials, Cambridge University Press, 2004.

[70] J. Freudenberger, M. Heilmaier, Materialkunde der Nichteisenmetalle und-legierungen, Wiley-VCH GmbH, 2020.

[71] H. Sun, K. Zhao, Electronic structure and comparative properties of LiNi$_x$Mn$_y$Co$_z$O$_2$ cathode materials, J. Phys. Chem. C 121 (11) (2017) 6002–6010.

[72] L.S. de Vasconcelos, R. Xu, J. Li, K. Zhao, Grid indentation analysis of mechanical properties of composite electrodes in Li-ion batteries, Extreme Mech. Lett. 9 (2016) 495–502.

[73] B. Wu, W. Lu, Mechanical modeling of particles with active core–shell structures for lithium-ion battery electrodes, J. Phys. Chem. C 121 (35) (2017) 19022–19030.

[74] R. Xu, H. Sun, L.S. de Vasconcelos, K. Zhao, Mechanical and structural degradation of LiNi$_x$Mn$_y$Co$_z$O$_2$ cathode in Li-ion batteries: An experimental study, J. Electrochem. Soc. 164 (13) (2017) A3333–A3341.

[75] Y. Yang, Q. Wu, Y. Cui, Y. Chen, S. Shi, R.-Z. Wang, H. Yan, Elastic properties, defect thermodynamics, electrochemical window, phase stability, and Li$^+$ mobility of Li$_3$PS$_4$: Insights from first-principles calculations, ACS Appl. Mater. Interfaces 8 (38) (2016) 25229–25242.

[76] A. Sakuda, A. Hayashi, M. Tatsumisago, Sulfide solid electrolyte with favorable mechanical property for all-solid-state lithium battery, Sci. Rep. 3 (1) (2013).

[77] C. Monroe, J. Newman, The impact of elastic deformation on deposition kinetics at lithium/polymer interfaces, J. Electrochem. Soc. 152 (2) (2005) A396.

[78] G.V. Samsonov (Ed.), Handbook of the Physicochemical Properties of the Elements, Springer US, 1968.

[79] D. Lide, CRC Handbook of Chemistry and Physics : A Ready-Reference Book of Chemical and Physical Data, CRC Taylor & Francis, Boca Raton, Fla, 2006.